J. Fluid Mech. (2004), *vol.* 516, *pp.* 349–377.
DOI: 10.1017/S0022112004000679 Printed in the United Kingdom

Transient and steady shapes of droplets attached to a surface in a strong electric field

By S. N. REZNIK, A. L. YARIN†, A. THERON AND E. ZUSSMAN

Faculty of Mechanical Engineering, Technion – Israel Institute of Technology, Haifa 32000, Israel

(Received 2 January 2003 and in revised form 18 March 2004)

The shape evolution of small droplets attached to a conducting surface and subjected to relatively strong electric fields is studied both experimentally and numerically. The problem is motivated by the phenomena characteristic of the electrospinning of nanofibres. Three different scenarios of droplet shape evolution are distinguished, based on numerical solution of the Stokes equations for perfectly conducting droplets. (i) In sufficiently weak (subcritical) electric fields the droplets are stretched by the electric Maxwell stresses and acquire steady-state shapes where equilibrium is achieved by means of the surface tension. (ii) In stronger (supercritical) electric fields the Maxwell stresses overcome the surface tension, and jetting is initiated from the droplet tip if the static (initial) contact angle of the droplet with the conducting electrode is $\alpha_s < 0.8\pi$; in this case the jet base acquires a quasi-steady, nearly conical shape with vertical semi-angle $\beta \leqslant 30^\circ$, which is significantly smaller than that of the Taylor cone ($\beta_T = 49.3^\circ$). (iii) In supercritical electric fields acting on droplets with contact angle in the range $0.8\pi < \alpha_s < \pi$ there is no jetting and almost the whole droplet jumps off, similar to the gravity or drop-on-demand dripping. The droplet–jet transitional region and the jet region proper are studied in detail for the second case, using the quasi-one-dimensional equations with inertial effects and such additional features as the dielectric properties of the liquid (leaky dielectrics) taken into account. The flow in the transitional and jet region is matched to that in the droplet. By this means, the current–voltage characteristic $I = I(U)$ and the volumetric flow rate Q in electrospun viscous jets are predicted, given the potential difference applied. The predicted dependence $I = I(U)$ is nonlinear due to the convective mechanism of charge redistribution superimposed on the conductive (ohmic) one. For $U = O(10kV)$ and fluid conductivity $\sigma = 10^{-4}\,\mathrm{S\,m^{-1}}$, realistic current values $I = O(10^2 nA)$ were predicted.

1. Introduction

Consider an axisymmetric droplet of an incompressible conducting viscous liquid on an infinite conducting plate. With gravity effects neglected, the stationary shape of the droplet is spherical. The droplet shaped as a spherical segment rests on the plate with a static contact angle of the liquid/air/solid system α_s (see figure 1*a*). Suppose that at the initial time moment $t = 0$ an electric potential is applied to the plate (and the droplet) relative to another plate located far from the first and parallel to it. Then at distances r from the droplet, much larger than its volume-equivalent

† Author to whom correspondence should be addressed: meralya@yarin.technion.ac.il

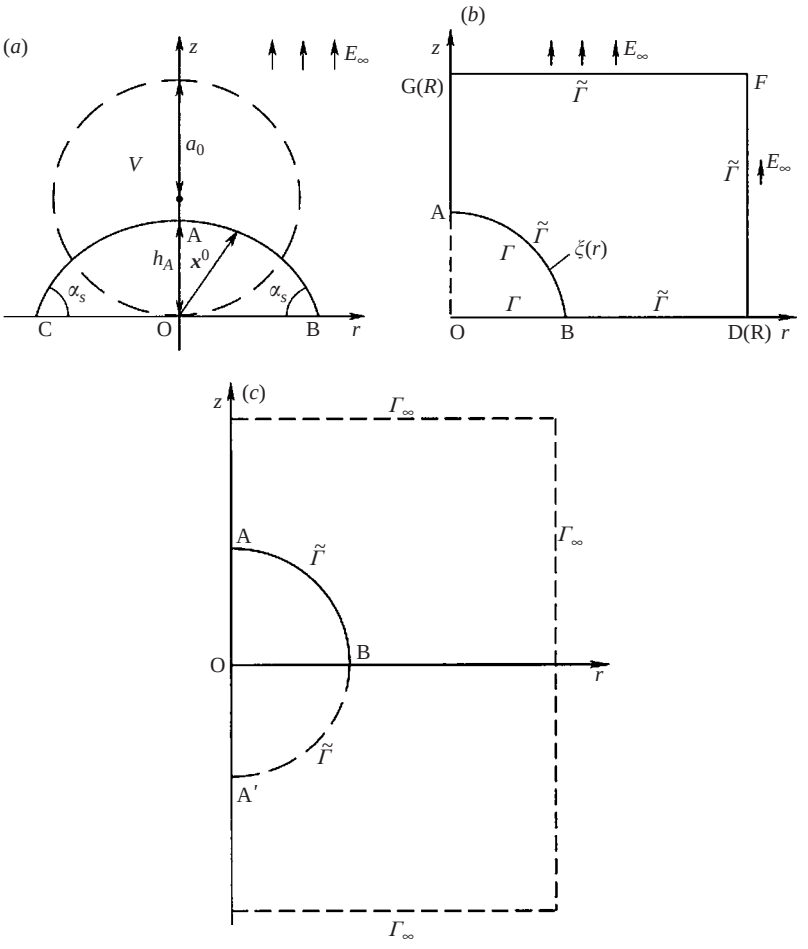

FIGURE 1. (*a*) The initial shape of the droplet at the moment when the electric field is to be applied. The dashed sphere represents the volume-equivalent droplet of volume V. (*b*) Sketch of the boundary curves Γ and $\tilde{\Gamma}$. (*c*) Sketch of the boundary curves $\tilde{\Gamma}$ and Γ_∞ used to eliminate any effect of the asymptotic boundary.

radius a_0 ($V = 4\pi a_0^3/3$, V being the droplet volume) a uniform field E_∞ is directed perpendicular to the plate (see figure 1*a*). The droplet is assumed to be initially at rest. With the field applied, the droplet evolves under the action of the electric, capillary and viscous forces. The aim of the present work is to determine the time pattern of this evolution.

The topicality of the problem is associated with such applications as electrospraying (Zeleny 1915, 1917; Cloupeau & Prunet-Foch 1989; Michelson 1990; Fernandez de la Mora 1992; Mestel 1994, 2002; Bailey 1998), pure liquid alloy ion sources (LAIS) (Forbes & Mair 1982; Prewett, Mair & Thompson 1982; Driesel, Dietzsch & Muhle 1996), and electrospinning of polymer nanofibres (Reneker & Chun 1996; Reneker *et al.* 2000; Yarin, Koombhongse & Reneker 2001*a*; Theron, Zussman & Yarin 2001). In all these cases an initially almost hemispherical droplet attached to a plate or an orifice is subjected to a strong capacitor-like electric field. As was shown in the seminal work of Taylor (1964), a conducting droplet raised above a critical electric potential

can no longer be sustained intact by surface tension, and jetting initiates from its tip. At the critical potential, according to Taylor (1964), infinite droplets acquire a conical shape with semi-angle $\beta_T = 49.3^\circ$ (the Taylor cone); Pantano, Ganan-Calvo & Barrero (1994) were the first to treat this issue for a finite drop attached to a tube. For dielectric droplets conical shapes with semi-angles $\beta < 49.3^\circ$ were predicted in Li, Halsey & Lobkovsky (1994). However, liquids could be considered as dielectrics only on time scales of the order of the charge relaxation time τ_C. For polymer solutions used in electrospinning, which are considered in the present work, $\tau_C \simeq 10^{-6}$ s, which is much shorter than the characteristic hydrodynamic time τ_H (cf. § 2). Therefore the results of Li *et al.* (1994) are inapplicable in the present situation. The recent experiments with electrospinning of Yarin, Koombhongse & Reneker (2001*b*) demonstrated critical cones with $\beta \approx 30^\circ$. Moreover, in the latter work it was shown theoretically that the Taylor cone corresponds to a self-similar solution of the Laplace equation for the electric potential, and there exist non-self-similar solutions (corresponding to acute, albeit rounded hyperboloids) which do not tend to the self-similar one. In the critical state these hyperboloids approach the value of $\beta \approx 33.5^\circ$. It seems that in the case of the elliptic Laplace equation self-similar solutions are not always attractive to the non-self-similar ones, as has already been demonstrated for the solutions of the biharmonic (with the Laplace operator squared) equation in the well-known Sternberg–Koiter paradox (Sternberg & Koiter 1958). This situation is completely different from the one associated with the parabolic boundary layer equations, where the self-similar solutions for jets (and plumes) originating from a point source (nozzle) are known to be attractive to the non-self-similar solutions for jets/plumes originating from finite-size nozzles/sources (Schlichting 1979; Zel'dovich 1992; Dzhaugashtin & Yarin 1977). Also, the self-similar system of surface-tension-dominated surface waves on a shallow liquid layer corresponding to a point initial perturbation and described by the beam equation with squared parabolic operator (Yarin & Weiss 1995) is definitely attractive for the corresponding non-self-similar waves. Indeed, the fact that the self-similar waves are realizable experimentally (Yarin & Weiss 1995) shows that the non-self-similar waves originating from non-point perturbations nevertheless tend to the self-similar ones in this case.

In the present work non-self-similar solutions for the electric and flow fields as well as the corresponding droplet shapes are sought. One of the aims is to check whether the non-self-similar solutions tend to that of Taylor (1964) at the critical steady state, or to a totally different critical equilibrium, as the approximate method of Yarin *et al.* (2001*b*) suggests. Moreover, since the calculations are done for the general transient situation, we expect to simulate the initiation of jetting from the droplet tip in the supercritical fields where the Maxwell stresses overcome the surface tension. In the past, numerical simulations of transient sub- and supercritical evolution of drops in electric fields have received much less attention than the static cases (Sherwood 1991; Notz & Basaran 1999; Suvorov & Litvinov 2000).

Electrospinning, mentioned above as the main motivation of the present work, is a straightforward, cheap and unique method to produce novel fibres with a diameter in the range of 100 nm or even less. To achieve this, polymer solutions are electrospun at a field strength of about $1\,\mathrm{kV\,cm^{-1}}$. The electric force results in jetting from the tip of a pendant or sessile droplet. After the jet has flown away from the droplet in a nearly straight line about 1 to 5 cm long, it bends in a complex path, during which electrical forces stretch and thin it by very large ratios. After the solvent evaporates, solid nanofibers are left. Theoretical studies of the key element of the electrospinning process, the bending instability of electrified jets, have been published

by Reneker *et al.* (2000), Yarin *et al.* (2001*a*), Shin *et al.* (2001) and Hohman *et al.* (2001*a*, *b*). The straight section of the electrospun jets was considered in Reneker *et al.* (2000), Hohman *et al.* (2001*a*) and Feng (2002). The numerous applications of electrospun nanofibers and mats include filter media, fiber-reinforced plastics, solar and light sails and mirrors in space, the application of pesticides to plants, cosmetic masks, biomedical applications (tissue engineering, scaffolds, bandages, drug release systems), protective clothing for biological and chemical protection, fibers loaded with catalysts and chemical indicators, and microaerodynamic decelerators and other airborne structures. They are of interest in the development of novel polymer-based light-emitting diodes, diodes, transistors, photonic crystals, flexible photocells, and for many other micro- and optoelectronic applications. Reviews devoted to the electrospinning process and its applications have been published by Fong & Reneker (2000), Yarin (2003), Frenot & Chronakis (2003) and Huang *et al.* (2003).

The subject of the present work is the droplet evolution and jet formation in electrospinning. The problem is posed in § 2. Non-dimensionalization is carried out in § 3. The numerical method is presented in § 4. The experimental setup is described in § 5. Comparison of the simulation results with the experimental data, and a discussion of them in the light of the numerical models known from the literature are given in § 6. Additional detailed numerical results are presented and discussed in § 7. The flow in a jet-like protrusion issuing from a droplet tip in sufficiently high electric fields is briefly discussed in § 8. The conclusions are formulated in § 9.

2. Problem formulation

Let us estimate the relevant characteristic dimensionless parameters of the problem. Take the liquid density $\rho \sim 1$ to $10\,\mathrm{g\,cm^{-3}}$, the viscosity $\mu \sim 10\,\mathrm{P}$, the surface tension $\gamma \sim 100\,\mathrm{g\,s^{-2}}$, the characteristic length $a_0 \leqslant 0.1\,\mathrm{cm}$, the characteristic velocity $V_0 = \gamma/\mu \sim 10\,\mathrm{cm\,s^{-1}}$. Then the Reynolds number is

$$Re = \frac{\rho V_0 a_0}{\mu} \leqslant 0.1 \text{ to } 1. \tag{1}$$

The parameter representing the relative importance of the electric and capillary stresses is the electric Bond number, defined as

$$Bo_E = \frac{a_0 E_\infty^2}{\gamma}. \tag{2}$$

Assume the applied electric field $E_\infty = 10/3$ to $100/3\,\mathrm{g^{1/2}\,cm^{-1/2}\,s^{-1}}$, which is 1 to $10\,\mathrm{kV\,cm^{-1}}$. Then $Bo_E = 10^{-2}$ to 1. In this case the electric stresses can compete with the surface tension and change the droplet shape significantly.

Note that in the present work all the equations that contain terms that depend on the electric field are expressed in Gaussian (CGS) units, and the values of all the parameters are given in CGS units. This is especially convenient and customary in cases where both electrostatics and fluid mechanics are involved. The values of the electric potential, the electric field strength, the electric current and conductivity are also converted to SI units for convenience.

The above values of Re enable us to consider the problem in the creeping-flow approximation up to the time when the velocity of the liquid $\boldsymbol{u}$ becomes much larger than V_0. The Stokes equations for the liquid motion within the droplet are

$$\nabla p = \mu \Delta \boldsymbol{u}, \tag{3}$$

$$\nabla \cdot \boldsymbol{u} = 0, \tag{4}$$

where $\boldsymbol{u} = (u_r, u_z)$ is the liquid velocity, and p is the pressure. Axial symmetry is assumed, Oz being the symmetry axis (cf. figure 1*a*).

The dynamic boundary conditions at the droplet surface are vanishing of the tangential stresses and balance of the normal stresses, with the effect of surface tension and electric stresses taken into account:

$$\boldsymbol{f} \cdot \boldsymbol{\tau} = 0, \tag{5}$$

$$\boldsymbol{f} \cdot \boldsymbol{n} = \gamma\kappa + \frac{E^2}{8\pi}. \tag{6}$$

Here $\boldsymbol{f}$ is the traction acting at a unit area of the liquid surface, $\boldsymbol{n}$ and $\boldsymbol{\tau}$ are the unit normal and tangent vectors at the surface; κ is the surface curvature. Note that $f_i = \Pi_{ik} n_k,\ i, k = \{r, z\}$ and

$$\Pi_{ik} = -p\delta_{ik} + \mu\left(\frac{\partial u_i}{\partial x_k} + \frac{\partial u_k}{\partial x_i}\right). \tag{7}$$

Since the liquid is assumed to be a perfect conductor, only the normal component of the field E is non-zero at the droplet surface. This assumption means that the characteristic charge relaxation time $\tau_C = \epsilon/(4\pi\sigma)$ is much less than its hydrodynamic counterpart $\tau_H = \mu a_0/\gamma$ (ϵ and σ being the dimensionless relative permittivity, or the dielectric constant, and conductivity of the liquid, respectively). The inequality $\tau_C/\tau_H \ll 1$ is equivalent to $\epsilon\gamma/(4\pi\sigma\mu a_0) \ll 1$. The latter obviously holds for liquid metals, as well as for the ionic conductors which are the main concern of the present work. In the latter case, we can take $\epsilon = 40$, $\mu = 20\,\mathrm{g\,cm^{-1}\,s^{-1}}$, $\gamma = 40\,\mathrm{g\,s^{-2}}$, $\sigma = 9 \times 10^5$ to $9 \times 10^6\,\mathrm{s^{-1}}$, which is 10^{-4} to $10^{-3}\,\mathrm{S\,m^{-1}}$, and $a_0 = 10^{-1}$ cm, which yield $\tau_C/\tau_H = 0.706 \times 10^{-5}$ to 0.706×10^{-4}.

To find the electric field E at the surface it is necessary to solve the Laplace equation for the electric potential Φ:

$$\Delta\Phi = \frac{\partial^2\Phi}{\partial r^2} + \frac{1}{r}\frac{\partial\Phi}{\partial r} + \frac{\partial^2\Phi}{\partial z^2} = 0, \tag{8}$$

$$\boldsymbol{E} = -\nabla\Phi = -\frac{\partial\Phi}{\partial r}\boldsymbol{e}_r - \frac{\partial\Phi}{\partial z}\boldsymbol{e}_z, \tag{9}$$

where $\boldsymbol{e}_r$ and $\boldsymbol{e}_z$ are the unit vectors in the radial and axial directions, respectively.

The boundary conditions for (8) are

$$\Phi = 0 \quad \text{at the drop surface } \xi(r) \text{ and at the plate COB in figure 1}(a), \tag{10}$$

and

$$-\frac{\partial\Phi}{\partial z} \to E_\infty \quad \text{as} \quad |\boldsymbol{r}| \to \infty, \tag{11}$$

where $\boldsymbol{r}$ is the position vector.

Then the electric field at the droplet surface S can be found as

$$E(\boldsymbol{x}) = -\frac{\partial\Phi}{\partial n}, \quad \boldsymbol{x} \in S, \tag{12}$$

where $\boldsymbol{x}$ is the position vector of the surface points at time t.

The kinematic boundary condition at the drop surface is

$$\frac{\mathrm{d}\boldsymbol{x}}{\mathrm{d}t} = \boldsymbol{u}(\boldsymbol{x}). \tag{13}$$

The solution of (13) is subject to the initial condition

$$\boldsymbol{x}(0) = \boldsymbol{x}^0, \tag{14}$$

where $\boldsymbol{x}^0$ is the position vector of the point at $t = 0$ (see figure 1*a*).

The no-slip boundary condition at the plate is

$$\boldsymbol{u} = 0, \;\; z = 0. \tag{15}$$

Note that this condition can be violated near the contact line (i.e. at points B and C in figure 1*a*). It is well known (Hoffman 1975; Dussan V. 1979; Cox 1986) that when the apparent contact angle α is not equal to the static contact angle α_s, then the contact line (CL) moves with a velocity depending on the values of the two angles α and α_s. However, this velocity is low relative to the characteristic velocity γ/μ and can be neglected (Reznik & Yarin 2002*a*, *b*, *c*; Reznik, Zussman & Yarin 2002). The latter is assumed in the present work, which means that the CL is immobilized throughout the drop evolution, whereas the angle α is free to change starting from $\alpha = \alpha_s$ at $t = 0$ (also cf. the experimental evidence in § 5).

3. Dimensionless parameters

Introduce the following dimensionless variables:

$$\overline{\boldsymbol{x}} = \frac{\boldsymbol{x}}{a_0}, \quad \overline{t} = \frac{t}{\tau_H}, \quad \overline{\boldsymbol{u}} = \frac{\boldsymbol{u}}{V_0}, \quad \overline{p} = \frac{a_0 p}{\gamma}, \quad \overline{\boldsymbol{E}} = \frac{\boldsymbol{E}}{E_\infty}, \quad \overline{\Phi} = \frac{\Phi}{E_\infty a_0}, \tag{16}$$

with the velocity scale $V_0 = \gamma/\mu$, and the time scale $\tau_H = \mu a_0/\gamma$.

The dimensionless dynamic boundary conditions (5) and (6) at the free surface of the droplet take the form

$$\boldsymbol{f} \cdot \boldsymbol{\tau} = 0, \tag{17}$$

$$\boldsymbol{f} \cdot \boldsymbol{n} = \kappa + \frac{Bo_E}{8\pi}\left(\frac{\partial \Phi}{\partial n}\right)^2. \tag{18}$$

Here and hereinafter the bars are dropped for convenience. The dimensionless boundary condition for the electric field is

$$-\frac{\partial \Phi}{\partial z} \to 1, \;\; |\boldsymbol{r}| \to \infty. \tag{19}$$

The dimensionless parameters representing the evolution of the droplet surface are then the electric Bond number Bo_E and the static contact angle α_s.

4. Numerical method

Equation (13) can be solved numerically using the Kutta–Merson method, provided the values $\boldsymbol{u}(\boldsymbol{x})$ are known for any given moment of time. These are found from the Stokes equations (3) and (4) with the boundary conditions (5), (6) and (15). The latter equations are equivalent to the following set of integral equations (Becker 1992; Pozrikidis 1992; van de Vorst 1994):

$$c_{ij}(\boldsymbol{x}_P)u_i(\boldsymbol{x}_P) = 2\pi \int_\Gamma f_i(\boldsymbol{x}_Q) G_{ij}^{axi}(\boldsymbol{x}_Q, \boldsymbol{x}_P) r_Q \, \mathrm{d}s - \mathrm{PV}\, 2\pi \int_\Gamma u_i(\boldsymbol{x}_Q) T_{ij}^{axi}(\boldsymbol{x}_Q, \boldsymbol{x}_P) r_Q \, \mathrm{d}s, \tag{20}$$

$\boldsymbol{x}_Q = (r_Q, z_Q)$, $\boldsymbol{x}_P = (r_P, z_P)$ being located at the boundary of the liquid volume Γ which incorporates the free surface of the droplet AB and its contact area with the plate BO in figure 1(*b*). The kernels G_{ij}^{axi} and T_{ij}^{axi} are expressed in terms of the complete elliptic integrals $K(m, \frac{1}{2}\pi)$, $E(m, \frac{1}{2}\pi)$ where

$$m = \frac{2\sqrt{r_P r_Q}}{C}, \quad C = \sqrt{(r_P + r_Q)^2 + (z_P - z_Q)^2}. \tag{21}$$

These expressions are given e.g. in Becker (1992); c_{ij} is a matrix with elements depending on the corner angle of the boundary curve Γ (see figure 1*b*) at point $\boldsymbol{x}_P$. The boundary is not necessarily supposed to be a Lyapunov curve (a Lyapunov curve has a continuously varying normal vector; Pozrikidis 1992). In (20) s is the parameter calculated along Γ.

To solve (20) we should find the tractions at the free liquid surface $\boldsymbol{f}$ induced by the surface tension and the electric field on the liquid surface (see (5) and (6)). To find the electric field it is necessary to solve (8) for the electric potential with the boundary conditions (10) and (11). Like (3) and (4), this equation is equivalent to the integral equation

$$c(\boldsymbol{x}_P)\Phi(\boldsymbol{x}_P) = 2\pi \int_{\widetilde{\Gamma}} \frac{\partial \Phi}{\partial n}(\boldsymbol{x}_Q) K_2^{axi}(\boldsymbol{x}_Q, \boldsymbol{x}_P) r_Q \, \mathrm{d}s - \mathrm{PV}\, 2\pi \int_{\widetilde{\Gamma}} \Phi(\boldsymbol{x}_Q) K_1^{axi}(\boldsymbol{x}_Q, \boldsymbol{x}_P) r_Q \, \mathrm{d}s, \tag{22}$$

where the kernels K_1^{axi} and K_2^{axi} are

$$K_2^{axi}(\boldsymbol{x}_Q, \boldsymbol{x}_P) = -\frac{1}{\pi^2 C} K\left(m, \frac{\pi}{2}\right), \quad K_1^{axi}(\boldsymbol{x}_Q, \boldsymbol{x}_P) = \frac{\partial K_2^{axi}(\boldsymbol{x}_Q, \boldsymbol{x}_P)}{\partial n_Q}. \tag{23}$$

$\widetilde{\Gamma}$ is the boundary incorporating the surface of the drop AB, the equipotential segment BD of the plate, the segments DF (where $\partial\Phi/\partial n = 0$) and FG (where $\partial\Phi/\partial n = -E_\infty$), located sufficiently far from the droplet (cf. figure 1*b*).

Solving (22) with the boundary conditions (10) and (11), we can find the electric field $E = -\partial\Phi/\partial n$ at the droplet surface for any surface shape.

Note, that if droplet is stretched strongly enough, or jetting has already begun at the droplet tip, the liquid surface could, in principle, approach the boundary GF in figure 1(*b*). However, any effect of this boundary can be easily eliminated. Introduce an auxiliary potential $\widetilde{\Phi}$:

$$\Phi = -E_\infty z + \widetilde{\Phi}. \tag{24}$$

According to the boundary conditions (10) and (11)

$$\widetilde{\Phi} = E_\infty \xi(r) \quad \text{at the drop surface } \xi(r), \tag{25}$$

$$\widetilde{\Phi} = O\left(\frac{1}{r^2}\right) \quad \text{as} \quad |\boldsymbol{r}| \to \infty \tag{26}$$

((26) corresponds to a dipole-like behaviour at infinity).

Potential $\widetilde{\Phi}$ satisfies the Laplace equation (8). Therefore, if we introduce a mirror image of the droplet as in figure 1(*c*), $\widetilde{\Phi}$ should satisfy the integral equation (22) with the integrals being evaluated over the boundary $\widetilde{\Gamma} + \Gamma_\infty$ (with $\widetilde{\Phi}$ at the droplet surface given by (25)). According to the boundary condition (26), the integrals over Γ_∞ vanish. After the derivative $\partial\widetilde{\Phi}/\partial n$ has been found from the integral equation,

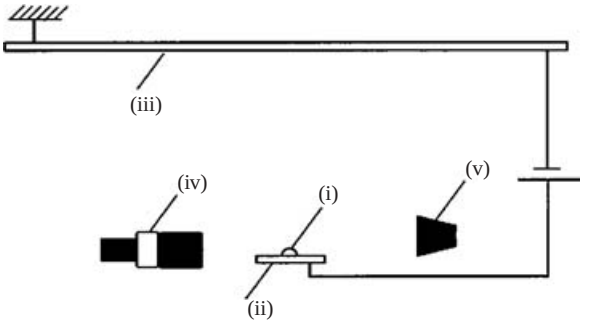

FIGURE 2. Experimental setup. (i) Sessile droplet of polymer solution; (ii) disk-like electrode attached to high voltage; (iii) grounded disk-like counter electrode; (iv) camera; (v) light source.

the electric field $E = E_\infty n_z - \partial\widetilde{\Phi}/\partial n$ at the droplet surface can be calculated for any surface shape ($n_z = \boldsymbol{n}\cdot\boldsymbol{e}_z$). Recourse to the electric potential $\widetilde{\Phi}$ eliminates any effect of the outer boundaries GF and FD and was always used in the calculations.

Equations (20) and (22) are solved using the boundary element method (BEM) described in detail in Becker (1992) and Pozrikidis (1992). For the numerical procedure we used a code based on Becker's BEACON, originally developed for two-dimensional elastostatic problems and modified for the potential and low-Reynolds-number hydrodynamic problems in the present work. At each time step the problem (8), (10) and (11) was solved for a known droplet shape. The electric field found was then substituted in (6) and the set (3)–(6) and (15) was solved. This yielded the velocity $\boldsymbol{u}$ of the points of the free surface. Then (13) was integrated to yield the time evolution of the free surface. A systematic increase of the number of quadratic boundary elements from 20 to 50 at the generatrix of the free surface of the droplet revealed almost identical droplet configurations for all the stages of evolution with a maximal cumulative shift in time of about 3.5%. Most of the calculations were done with 50 boundary elements at the generatrix of the free surface of the droplets.

5. Experimental setup

The experimental apparatus allowed observation of droplet evolution under conditions close to those implemented for the numerical simulations (figure 2). Sessile droplets (i) of polymer solutions were located at the centre of a disk-like electrode (ii) of radius $a_e = 0.6$ cm. The electrode was attached to high voltage of $\Phi_0 = 12$ to 18 kV at the moment $t = 0$. The initial droplet shapes (before the high voltage was applied) were fairly close to spherical segments of radii $a_0 \simeq 0.1$ cm (droplet volume was of the order of 10 µl). At a distance of 5 cm above (ii), a parallel grounded disk-like counter electrode (iii) of radius $a_{ce} = 5.5$ cm was located. Droplet evolution in time was imaged with an electronic camera (iv) (MotionScope – Redlake Imaging Corporation). The camera speed was 2000 f.p.s. and the shutter speed 0.05 ms. The camera was equipped with a 70–180 mm, $f/4.5$ zoom lens. The light source (v) (400 W HMI lamp with Dedolight DEB400D electronic ballast) was placed against the camera along its line of sight. Polymers used were Poly(ethylene oxide) (PEO) of molecular weights $M_w = 6 \times 10^5$ and 10^6 g mol^{-1} (Aldrich) and Polycaprolactone (PCL), of molecular weight of $M_w = 8 \times 10^4$ g mol^{-1} (Aldrich). Four different solutions were tested: (i) 3% wt PEO ($M_w = 6 \times 10^5$ g mol^{-1}) in ethanol/water (40/60 mixture) (called solution PEO1). (ii) 3% wt PEO ($M_w = 10^6$ g mol^{-1}) in ethanol/water (40/60

Solution	ϵ	σ (S m^{-1})	γ (g s^{-2})
PEO1	61.44	1.38×10^{-3}	37
PEO2	67.97	1.28×10^{-3}	38
PCL1	25.38	0.141×10^{-3}	23
PCL2	21.3	0.273×10^{-3}	28.9

TABLE 1. Material properties of the solutions used in the experiments.

mixture) (PEO2), (iii) 10% wt PCL in acetone (PCL1), (iv) 8% wt PCL in Methylene chloride (MC)/Toluene 75/25 mixture (PCL2). The permittivity, conductivity and surface tension of the solutions are given in table 1.

At the relatively low rates of deformation characteristic of the flow inside droplets prior to jetting, which are of the order of $10^{-1}\,\mathrm{s}^{-1}$, the rheological behaviour of these polymer solutions is close to that of viscous Newtonian fluids and can be characterized by zero-shear viscosity μ. Measurements of the zero-shear viscosities revealed values of μ of the order of 10 or 10^2 P. The results can be considered only as an order of magnitude estimate due to the inaccuracies usually involved in zero-shear viscosity measurements (a Couette programmable viscometer Brookfield DV-II+ was used), and also due to the fact that solvent evaporation during the experiment could lead to an increase of viscosity. Discussion of the effective values of viscosity for the experiments will be given in § 6.

Droplets were released at the disk-like electrode from a syringe and acquired steady-state shapes fairly close to those of spherical segments with the corresponding static contact angles. Then, at time $t = 0$ a high voltage was instantaneously applied and droplet evolution was recorded by the camera. The results for PCL2 are presented in figure 3. No visible motion of the contact line was recorded. Axial symmetry of the flow was fairly accurately sustained during the whole droplet evolution. Limited camera resolution did not allow reliable recording of the very tip of the droplets prior to jetting (figure 3). Therefore recorded droplet heights are typically slightly underestimated. However, the jetting onset is clearly seen. The jetting of PEO1 droplet starts at $t_{jet} = 609.5$ ms, of PEO2 at $t_{jet} = 1247$ ms, of PCL1 at $t_{jet} = 535$ ms, and of PCL2 at $t_{jet} = 756.5$ ms (figure 3).

Experiments on drop evolution in a high-voltage electric field were conducted by Zhang & Basaran (1996). They used low-viscosity fluid (water), and droplets were attached to a capillary. The flow behaviour of the droplets was quite distinct from that of the highly viscous fluids used for electrospinning of nanofibers. Also, the boundary condition (attachment to a capillary filled by fluid) was different from the one considered in the present work. Thus it was impossible to use the data of Zhang & Basaran (1996) for comparison and there was a need to conduct the present set of experiments.

6. Comparison of the simulations with the experimental data and other numerical models

Consider a conducting disk of radius a_e charged by a charge e. The potential of the electric field in the whole space is given by (Landau & Lifshitz 1995)

$$\Phi = \frac{e}{a_e} \arctan \left\{ \frac{2a_e^2}{r^2 + z^2 - a_e^2 + \left[\left(r^2 + z^2 - a_e^2 \right)^2 + 4a_e^2 z^2 \right]^{1/2}} \right\}^{1/2}. \qquad (27)$$

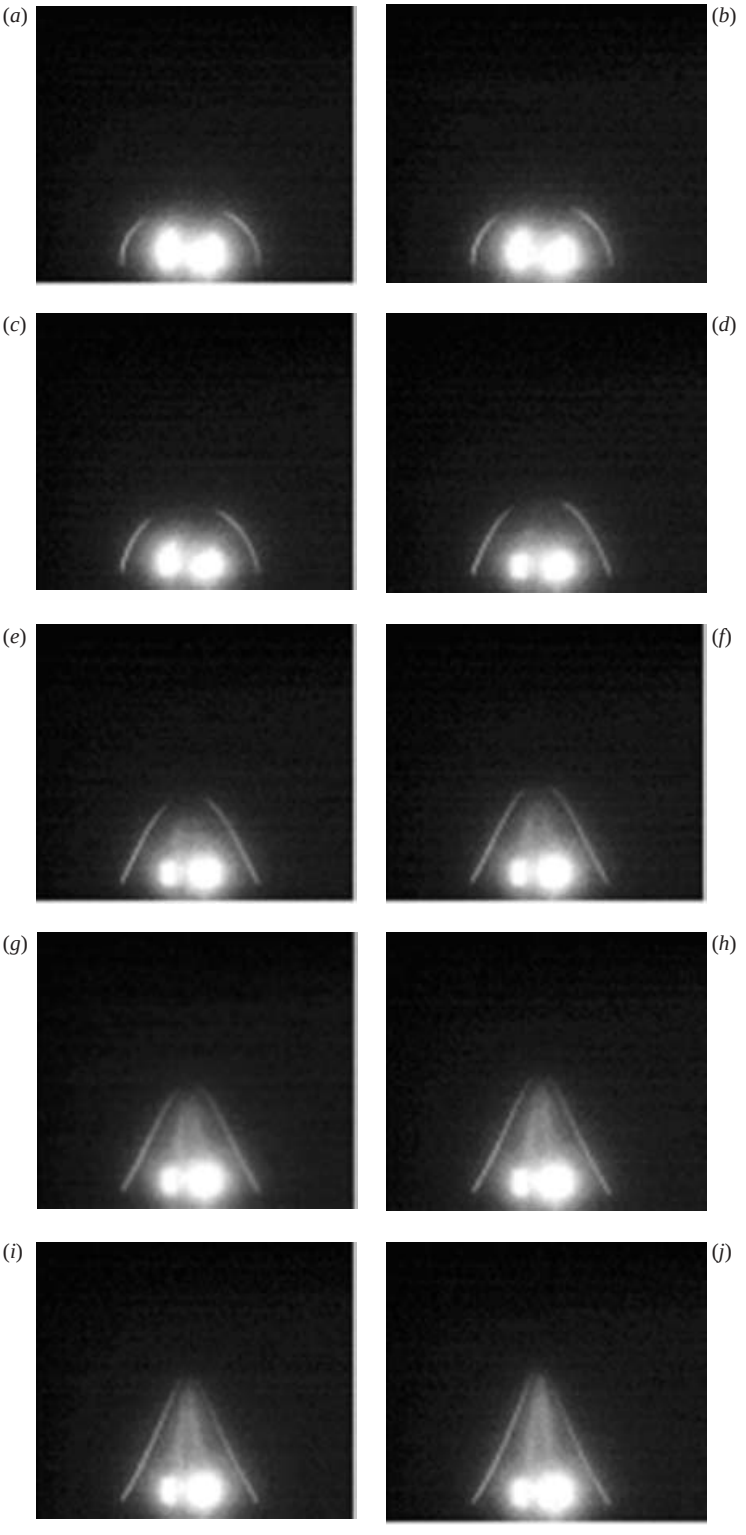

FIGURE 3. Evolution of a PCL2 droplet. Applied voltage is 13.5 kV, droplet volume is about 10 μl. Times are the following: (*a*) 0 ms, (*b*) 101.5 ms, (*c*) 201.5 ms, (*d*) 351.5 ms, (*e*) 501.5 ms, (*f*) 601.5 ms, (*g*) 651.5 ms, (*h*) 701.5 ms, (*i*) 731.5 ms, (*j*) 756.5 ms.

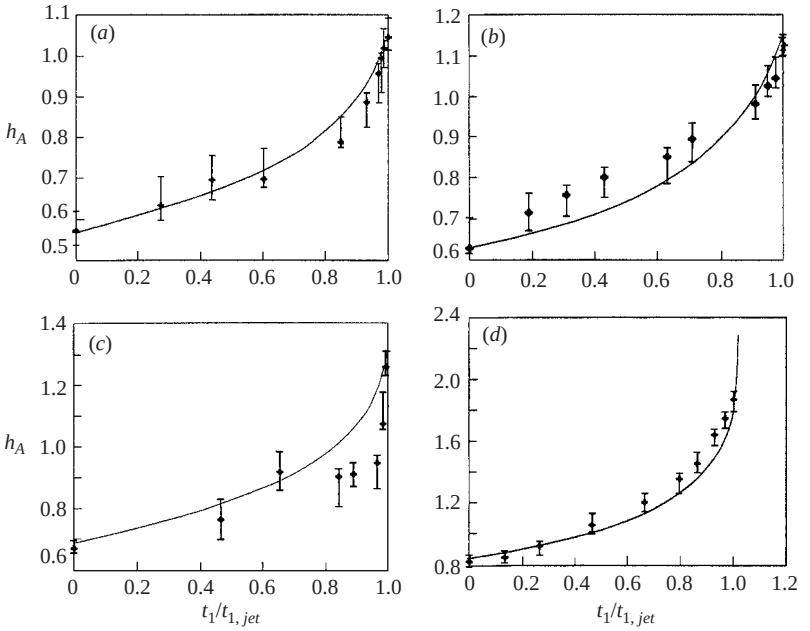

FIGURE 4. The tip height normalized by a_0 versus time normalized by the jetting time. (*a*) PEO1 droplet. (*b*) PEO2 droplet, (*c*) PCL1 droplet, (*d*) PCL2 droplet. The symbols show the experimental data, the curves the computational predictions.

Therefore

$$\Phi_o = \Phi|_{z=0} = \frac{\pi e}{2a_e}. \tag{28}$$

The charge density at the centre of the disk surface $q_e = e/(4\pi a_e^2)$, and the normal field strength $E_n = 4\pi q_e$. For a tiny droplet located at the disk centre E_n is identical to E_∞ of § 2, which allows an estimate of the field strength corresponding to the applied voltage

$$E_\infty = \frac{2}{\pi}\frac{\Phi_o}{a_e} \tag{29}$$

(use is made of (28)).

The electric Bond number in (2) for the experiments becomes

$$Bo_E = \frac{a_0}{\gamma}\frac{4\Phi_0^2}{(\pi a_e)^2}. \tag{30}$$

Taking $\gamma = 40\,\mathrm{g\,s^2}$, $a_e = 0.6\,\mathrm{cm}$, $a_0 = 10^{-1}\,\mathrm{cm}$ and $\Phi_0 = 50\,\mathrm{g^{1/2}\,cm^{1/2}\,s^{-1}}$, which is 15 kV, we obtain $Bo_E \sim 7$. For such high values of the electric Bond number the effect of the surface tension is rather small and jetting is inevitable. In fact, for $Bo_E \gg 1$ surface tension could be neglected in the calculations from the very beginning. This means that for $Bo_E \gg 1$ the characteristic time is $\tau_E = \mu/E_\infty^2$ instead of τ_H.

The results of the numerical calculations are compared to the experimental data of § 5 in figures 4 and 5. The droplet boundaries were estimated through image processing using Adobe Photoshop and Matlab. The image calibration was done using a wire of known width photographed at the same record rate and shutter speed as the droplet. In figure 4(*a–d*) the tip height is plotted as a function of time for PEO1,

PEO2, PCL1 and PCL2, respectively. In the figures dimensionless time $t_1 = t/(\mu/E_\infty^2)$ is scaled by the dimensionless jetting time $t_{1,jet} = t_{jet}/(\mu/E_\infty^2)$, which is equal to 9.2, 11, 7.83 and 8.14 for PEO1, PEO2, PCL1 and PCL2, respectively (all the values are computational). The effective viscosity could be estimated from the equality of the dimensional jetting time in the calculations and in the experiments. Therefore for PEO1 $9.2\mu/E_\infty^2 = 0.6095$ s, for PEO2 $11\mu/E_\infty^2 = 1.247$ s, for PCL1 $7.83\mu/E_\infty^2 = 0.535$ s, and for PCL2 $8.14\mu/E_\infty^2 = 0.7565$ s. In all cases E_∞ is calculated from (29), which yields $E_\infty = 58.35, 63.66, 42.44$ and $47.75\,\mathrm{g}^{1/2}\,\mathrm{cm}^{-1/2}\,\mathrm{s}^{-1}$ for PEO1, PEO2, PCL1 and PCL2, respectively. Therefore the estimate yields $\mu = 225, 459, 123$ and $212P$ for PEO1, PEO2, PCL1 and PCL2, respectively. These values are plausible in the light of the estimates of zero-shear viscosity following from the measurements mentioned in § 5. The higher value of μ found for PEO2 compared to that for PEO1 is consistent with the fact that the molecular weight of PEO2 is higher than that of PEO1 (polymer concentrations and solvents are the same in both cases).

As was mentioned in § 5, the experimental values of the tip height h_A are typically underestimated. That might be the reason for a significant difference between the predicted and measured values seen in figure 4(*c*). In figures 4(*a*), 4(*b*) and 4(*d*) the agreement between the predictions and measurements is fairly satisfactory.

In figure 5 the predicted and measured shapes of the PCL2 droplet are shown at different time moments. The results correspond to those of figure 4(*d*). In this case the theory slightly underestimates the stretching rate, but the overall agreement is fairly good. The shift could be attributed to the neglect of inertia in the calculations. However, that is not the case: the values of the tip velocity u_z measured in the experiments are: for curve (i) in figure 5 $0\,\mathrm{cm\,s^{-1}}$, (ii) $0.058\,\mathrm{cm\,s^{-1}}$, (iii) $0.110\,\mathrm{cm\,s^{-1}}$, (iv) $0.142\,\mathrm{cm\,s^{-1}}$, (v) $0.167\,\mathrm{cm\,s^{-1}}$, (vi) $0.221\,\mathrm{cm\,s^{-1}}$, (vii) $0.353\,\mathrm{cm\,s^{-1}}$, (viii) $0.485\,\mathrm{cm\,s^{-1}}$, (ix) $0.638\,\mathrm{cm\,s^{-1}}$, (x) $0.941\,\mathrm{cm\,s^{-1}}$; the corresponding values in the calculations are quite similar. The viscosity of PCL2 $\mu = 212$ P, the density $\rho \simeq 1.32\,\mathrm{g\,cm^{-3}}$, and the droplet size $a_0 \simeq 0.1$ cm. Therefore the highest value of the Reynolds number corresponding to figure 8 is $Re = 5.86 \times 10^{-4}$, which hardly gives any inertial effects.

Note also, that the assumed initial shape of the droplet as a spherical segment (which is similar to Harris & Basaran 1993) slightly differs from the actual droplet shape near the contact line, presumably due to squeezing by the gravity force. This discrepancy should not have any significant effect on droplet evolution, since the Maxwell stresses pulling the droplet are almost fully determined by the tip shape, which is reproduced rather accurately.

Several recent numerical works are devoted to close, but different cases. For example, Wohlhuter & Basaran (1992) using finite-element analysis calculated steady-state shapes of pendant/sessile droplets in an electric field. Their droplets, however, were considered as polarizable dielectrics (non-conductors) with no free charges embedded at the free surface. In the situation considered in the present work the fluid behaviour corresponds to that of ionic conductors (cf. § 2). Therefore neither the electric context in the present work, nor the dynamic and static droplet shapes can be related to those predicted in Wohlhuter & Basaran (1992).

Harris & Basaran (1993) calculated static shapes of conducting drops hanging from a protruding nozzle or one submerged in the wall, filled by fluid. The nozzle was attached to an electrode of a parallel-plate capacitor – an electrical field slightly different from the one considered in the present work. The boundary conditions are also different from those for the sessile droplets at a solid wall considered in the present case; however, their prediction of the critical semi-angle $\beta < 40°$,

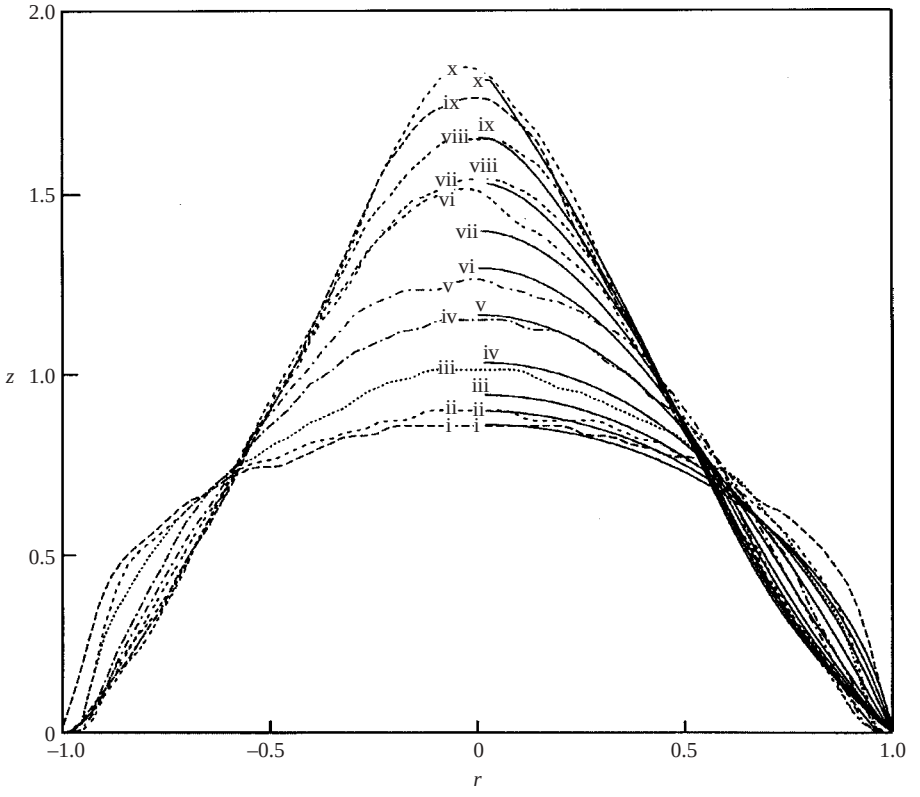

FIGURE 5. Measured and predicted shapes of the PCL2 droplet at different time moments: i $t = 0$, ii 101.5, iii 201.5, iv 351.5, v 501.5, vi 601.5, vii 651.5, viii 701.5, ix 731.5, x 756.5. Time is given in ms. The calculation results are shown by solid lines for the right-hand side of the droplet only. Their numerals are located at their tip points (corresponding to $r = 0$). The experimental shapes are plotted as dotted lines. On the left-hand side the values of r are artificially made negative.

which is significantly smaller than $\beta_T = 49.3°$, is quite remarkable. An additional comparison of that work with the static results of the present one is given below in § 7.

Notz & Basaran (1999) carried out a numerical analysis of drop formation from a tube in an electric field. Again, the boundary condition is quite different from the present case. Moreover, the flow in the drops was treated as an inviscid potential flow. In a subcritical electric field when no jetting is initiated such a model predicts undamped oscillations of the droplet. Obviously, such a behaviour, as well as that in jetting, is incompatible with the creeping flow case of the present work corresponding to the estimates of § 2.

Electrostatically levitated droplets could also develop pointed ends and jetting at the poles. Calculations for inviscid or slightly viscous fluids have demonstrated a tendency to protrusion development at the droplet poles in strong electric fields (Haywood, Renksizbulut & Raithby 1991; Basaran *et al.* 1995; Feng & Leal 1996). Experiments, also corresponding to the low-viscosity limit, have revealed thin jets issuing from droplet poles and totally disintegrating during 5 μs (Duft *et al.* 2003). None of these cases is comparable to the present one dominated by the high viscosity characteristic of spinnable polymer solutions.

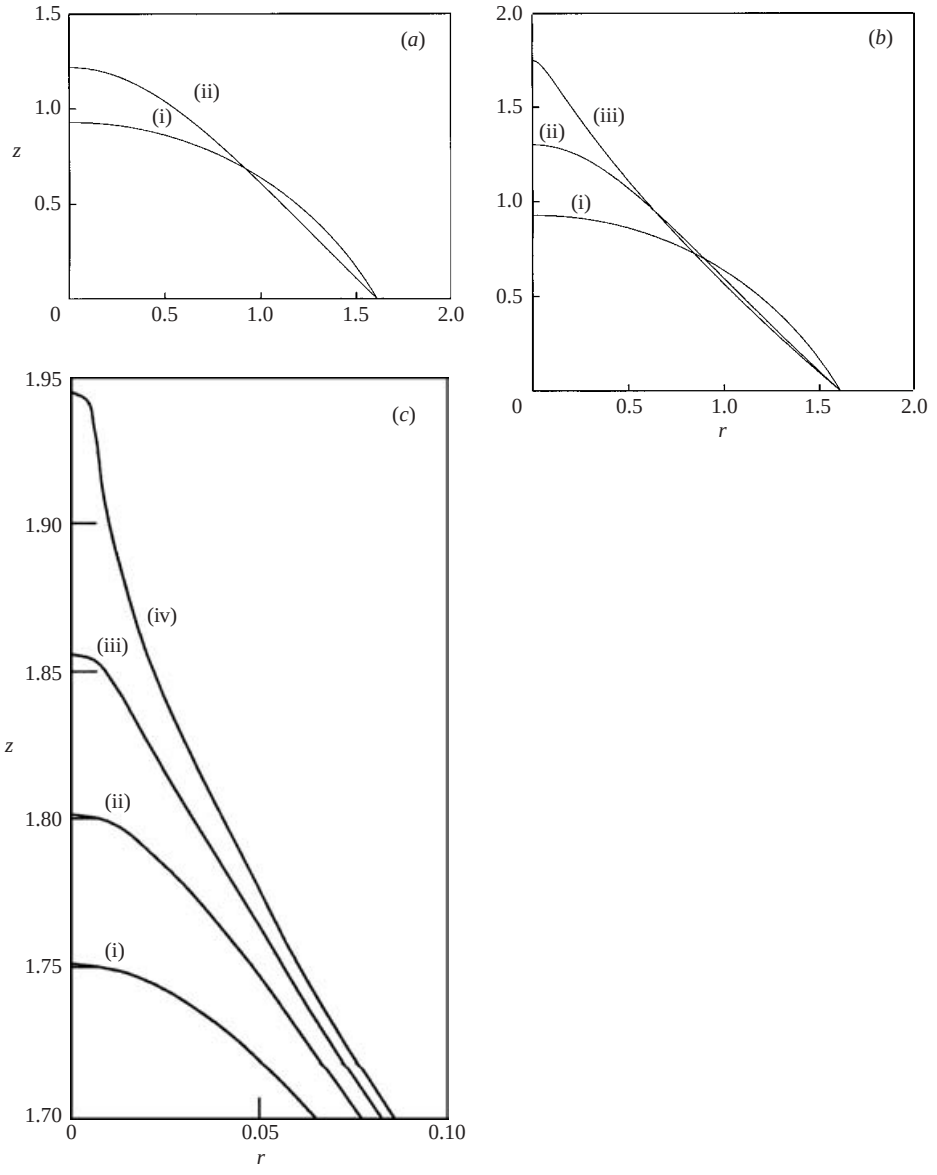

FIGURE 6. Droplet evolution corresponding to the contact angle $\alpha_s = \pi/3$; (*a*) $Bo_E = 5.06$: the subcritical case, curve (i) shows the initial droplet shape at $t = 0$, (ii) the saturated shape at $t = 16$; (*b*) $Bo_E = 5.29$: the initial stage of the supercritical case, (i) $t = 0$, (ii) $t = 13.7$, (iii) $t = 21.4$; (*c*) the jetting stage emerging in the supercritical case, (i) $t = 21.4$, (ii) 21.417, (iii) 21.426, (iv) 21.433.

7. Additional numerical results and discussion

The time evolution of the droplet surface, found numerically for $\alpha_s = \pi/3, \pi/2, 2\pi/3$ and 0.8π at different values of Bo_E is illustrated in figures 6 to 9. The corresponding time dependence of the tip height of the drop $h_A(t)$ is shown in figure 10. It is seen that the initially spherical droplet deforms under the action of the electric stresses and the tip moves upward. This is because the electric charge density near the tip is

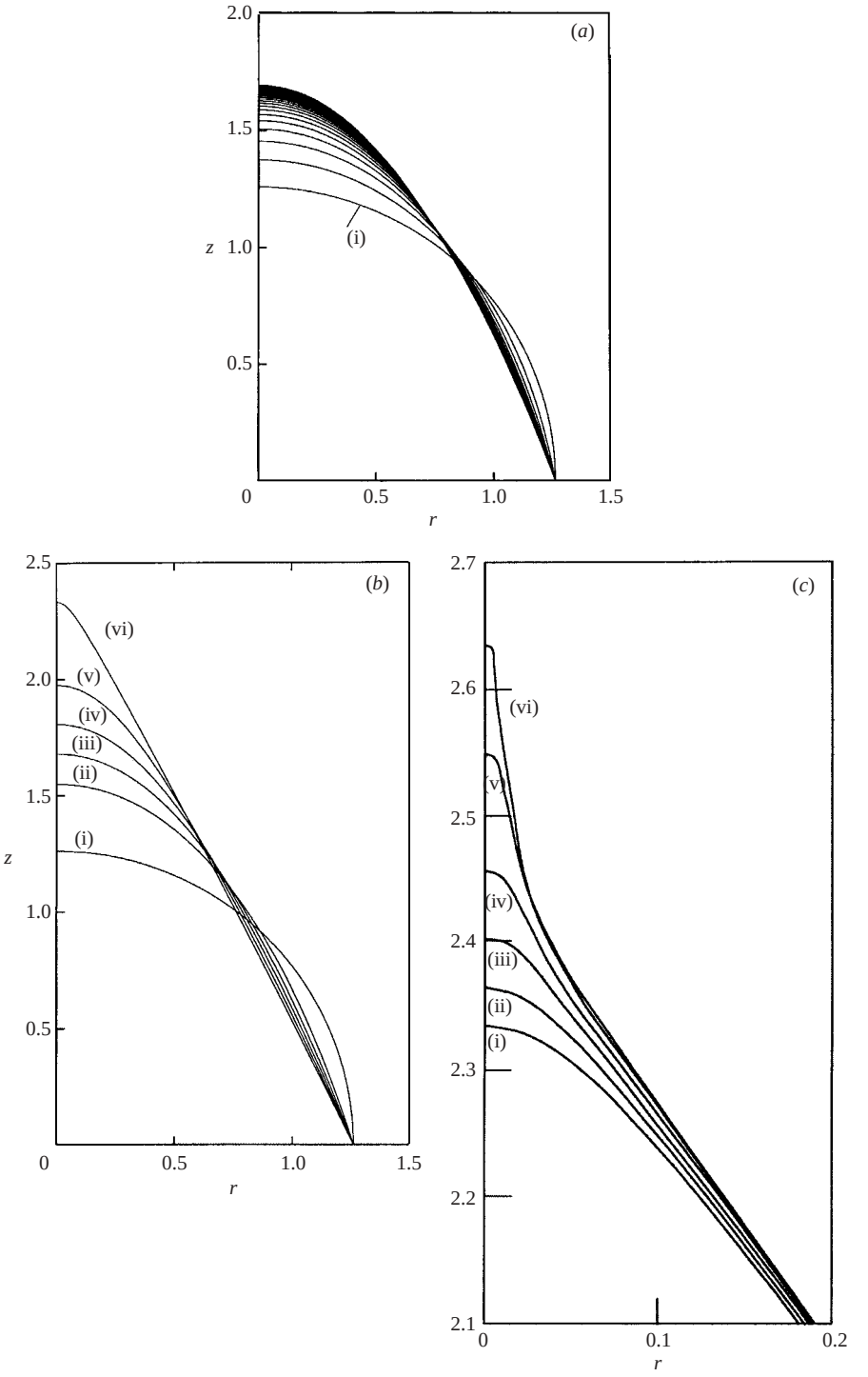

FIGURE 7. Droplet evolution corresponding to the contact angle $\alpha_s = \pi/2$; (*a*) $Bo_E = 3.03$: the subcritical case, curve (i) shows the initial droplet shape at $t = 0$, the subsequent curves correspond to the time intervals $\Delta t = 1$; (*b*) $Bo_E = 3.24$: the initial stage of the supercritical case, (i) $t = 0$, (ii) $t = 3$, (iii) $t = 6$, (iv) $t = 9$, (v) $t = 11$, (vi) $t = 12$; (*c*) the jetting stage emerging in the supercritical case, (i) $t = 12.001$, (ii) 12.012, (iii) 12.022, (iv) 12.03, (v) 12.037, (vi) 12.041.

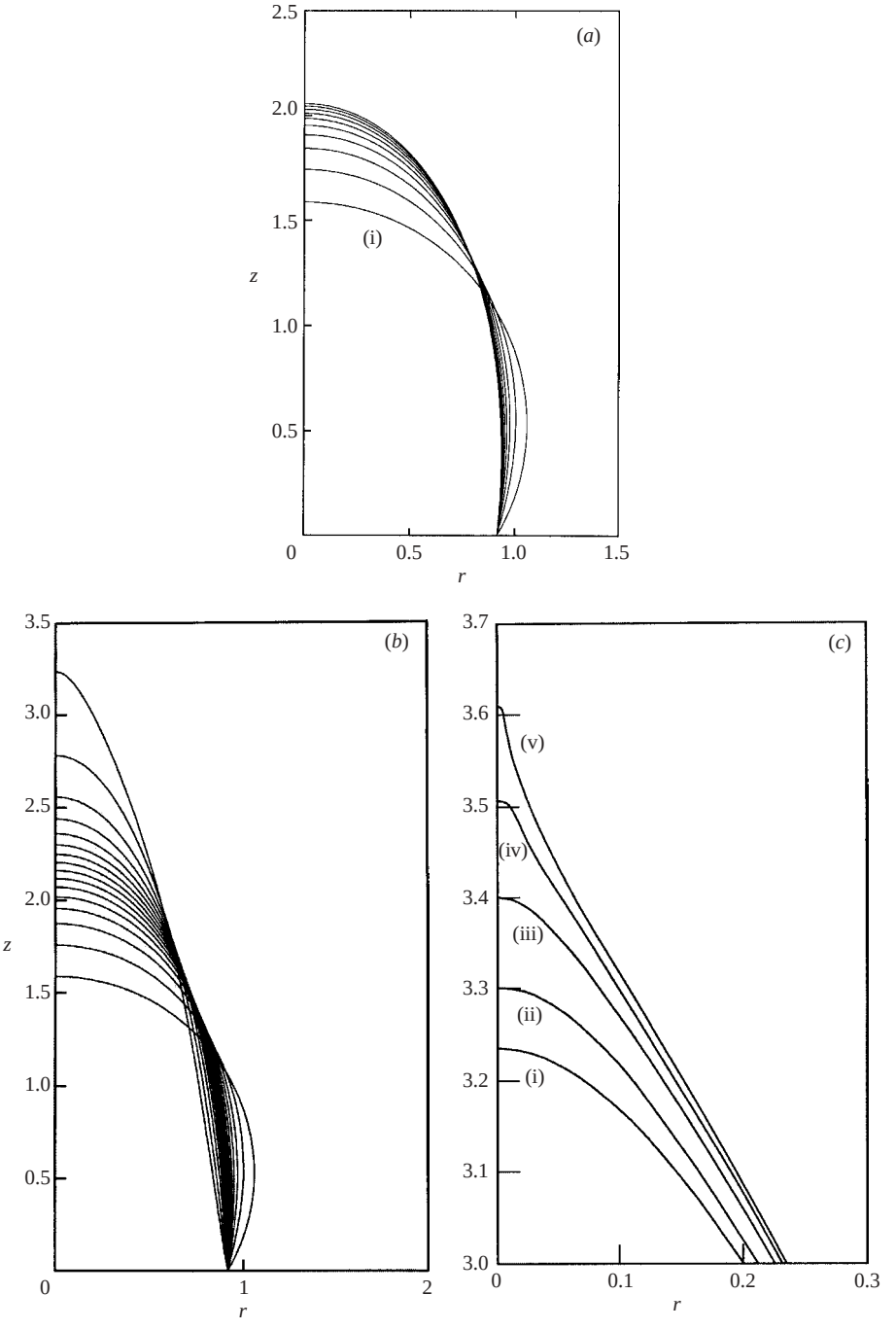

FIGURE 8. Droplet evolution corresponding to the contact angle $\alpha_s = 2\pi/3$; (*a*) $Bo_E = 1.82$: the subcritical case, curve (i) shows the initial droplet shape at $t = 0$, the subsequent curves correspond to the time intervals $\Delta t = 1$ until the droplet shape virtually saturates; (*b*) $Bo_E = 1.96$: the initial stage of the supercritical case, the bottom shape corresponds to $t = 0$, the subsequent curves correspond to the time intervals $\Delta t = 1$; (*c*) the jetting stage emerging in the supercritical case, (i) $t = 14.701$, (ii) 14.741, (iii) 14.782, (iv) 14.803, (v) 14.818.

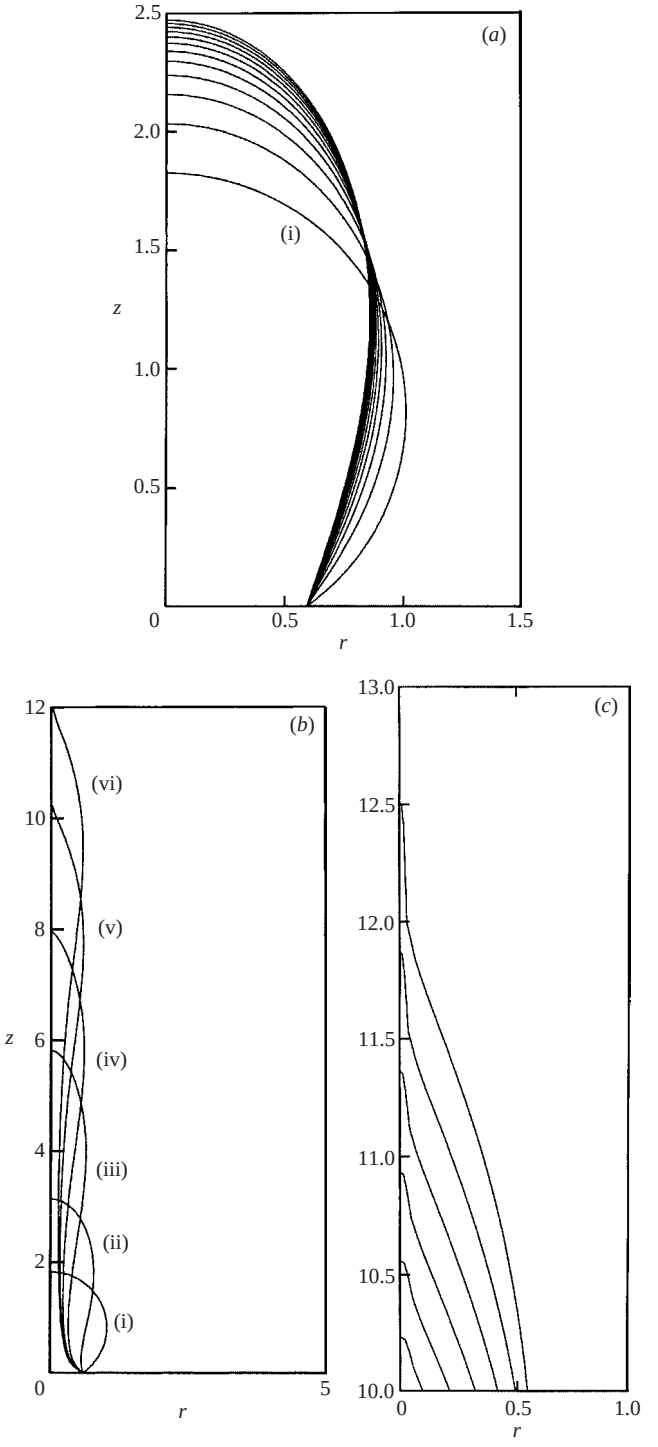

FIGURE 9. Droplet evolution corresponding to the contact angle $\alpha_s = 0.8\pi$; (*a*) $Bo_E = 1.21$: the subcritical case, curve (i) shows the initial droplet shape at $t = 0$, the subsequent curves correspond to the time intervals $\Delta t = 1$ until the droplet shape virtually saturates; (*b*) $Bo_E = 2.25$: the initial stage of the supercritical case, (i) $t = 0$, (ii) 2, (iii) 2.55, (iv) 2.6, (v) 2.614, (vi) 2.619, (*c*) the jetting stage emerging in the supercritical case, the bottom shape corresponds to $t = 2.614$, the subsequent curves correspond to the time intervals $\Delta t = 0.001$.

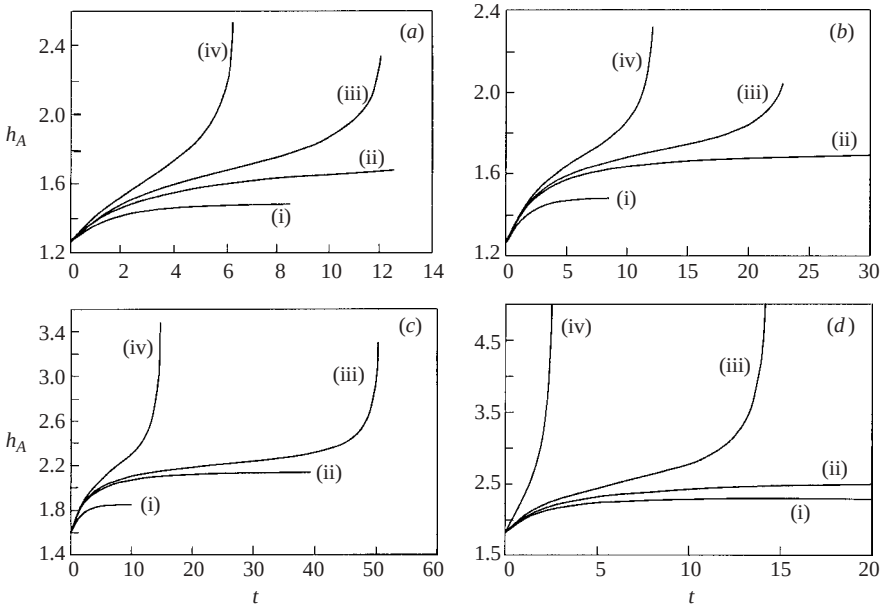

FIGURE 10. The tip height versus time (*a*) $\alpha_s = \pi/3$, (i) $Bo_E = 4.41$, (ii) $Bo_E = 5.06$, (iii) $Bo_E = 5.29$, (iv) $Bo_E = 6.25$ (cases i and ii subcritical, iii and iv supercritical jetting); (*b*) $\alpha_s = \pi/2$, (i) $Bo_E = 2.56$, (ii) $Bo_E = 3.03$, (iii) $Bo_E = 3.1$, (iv) $Bo_E = 3.24$ (cases i and ii subcritical, iii and iv supercritical jetting); (*c*) $\alpha_s = 2\pi/3$, (i) $Bo_E = 1.44$, (ii) $Bo_E = 1.82$, (iii) $Bo_E = 1.85$, (iv) $Bo_E = 1.96$; (cases i and ii subcritical, iii and iv supercritical jetting) (*d*) $\alpha_s = 0.8\pi$, (i) $Bo_E = 1.1$, (ii) $Bo_E = 1.2$, (iii) $Bo_E = 1.3$, (iv) $Bo_E = 2.25$ (cases i and ii subcritical, iii and iv supercritical jetting).

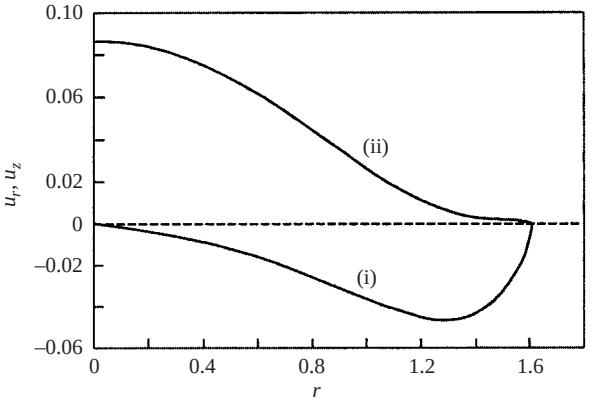

FIGURE 11. The radial (curve i) and vertical (curve ii) velocity components at the droplet surface versus r for $\alpha_s = \pi/3$ and $Bo_E = 5.29$ at $t = 0$. Note that in the creeping flow approximation flow arises immediately at $t = 0$.

higher than elsewhere (Yarin *et al.* 2001*b*) and, as a result, the electric stresses also concentrate there. Thus, the resultant pressure (the sum of the electric and capillary ones) near the tip is less that far from the tip where the electric charge density is small. Subject to the corresponding pressure gradient the liquid moves upward, towards the tip. The vertical velocity component at the surface is maximal at the tip and decreases as the distance from it increases (figure 11).

The results presented in figures 6 to 10 show that as the droplet surface becomes more tapered near the tip, the surface tension becomes more able to compete with the electric force if the value of Bo_E is not very large. As a result, the tip velocity $\mathrm{d}h_A/\mathrm{d}t$ decreases during the intermediate time interval (cf. figure 10). The subsequent evolution of the droplet depends on the value of the parameter Bo_E. For sufficiently small (subcritical) values, the tip velocity decreases monotonically with time and tends to zero as $t \to \infty$ (cf. curves i and ii in figure 10*a–d*). On the other hand, jetting sets in at the tip for sufficiently large values of Bo_E (cf. curves iii and iv in figure 10*a–d*).

The subcritical range of Bo_E depends on the value of the static contact angle α_s: for $\alpha_s = \pi/3$ we found $5.14 < Bo_{E,cr} < 5.15$; for $\alpha_s = \pi/2$, $3.03 < Bo_{E,cr} < 3.04$; for $\alpha_s = 2\pi/3$, $1.83 < Bo_{E,cr} < 1.84$; and for $\alpha_s = 0.8\pi$, $1.21 < Bo_{E,cr} < 1.22$. For $Bo_E < Bo_{E,cr}$ stationary droplet configurations emerge, in which the absolute values of the curvature of the free surface are maximal at the tip and decrease as the distance from it increases. The static surface is convex everywhere for sufficiently large α_s (see figure 8*a*), but it can also be concave far from the tip for small α_s (cf. figure 6*a*).

Some of the static results can be compared with the predictions for a drop hanging from a nozzle submerged in one of the electrodes of a parallel-plate capacitor in Harris & Basaran (1993). The effective dimensionless potential P used in that work is related to the present electric Bond number as $P = [2^{1/3} Bo_E/(8\pi)]^{1/2} H$, where H is the dimensionless distance between the capacitor electrodes, and a_0 in (2) is taken as the volume-equivalent drop radius. In the case of $\alpha_s = \pi/2$ (equivalent to $D = 0$ in Harris & Basaran 1993) our $Bo_{E,cr} = 3.03$ to 3.04. Therefore our prediction for P_{cr} in the case $H = 10$ is $P_{cr} = 3.9$. The same value can be found in figure 3 in Harris & Basaran (1993). The corresponding critical aspect ratio for the drop predicted in the latter work is about 1.36, while the one calculated here is 1.353. The maximum surface charge density is 0.56 (figure 21 in Harris & Basaran 1993) and 0.52 in our case.

The duration t_E of the evolution to the steady state increases with Bo_E (see curves i and ii in figure 10*a–d*). For example, $t_E \simeq 8$ for $Bo_E = 1.44$, and $t_E \simeq 20$ for $Bo_E = 1.82$ (for $\alpha_s = 2\pi/3$; cf. figure 10*c*).

At moderate supercritical values of the Bond number another scenario is realized. The tip velocity reaches a minimum at some intermediate moment of time and then begins to increase once more (curves iii and iv in figure 10*a–d*). For sufficiently large Bond numbers the tip velocity increases monotonically with time. The corresponding shapes of the free surface are shown in figures 6(*b*, *c*) to 9(*b*, *c*). It is seen that after long times the shape near the tip tends to a cone with a thin jet issuing from it. The time of the evolution from the initial equilibrium state to the moment of jet emergence decreases steeply as the supercritical value of Bo_E increases for a fixed α_s, while the shape of the surface at that moment remains practically unchanged over a wide range of variation of Bo_E. As is seen in figure 12, the height of the droplet tip increases as Bo_E increases from 5.29 to 25. However, the increase is relatively small and the vertical semi-angle remains about $\beta \simeq 30^\circ$.

The fact that the droplet shape at the moment of jet emergence hardly depends on the value of Bo_E can be explained as follows. For a sufficiently large Bo_E capillarity can be neglected compared to the Maxwell stresses, and (18) reduces to

$$\boldsymbol{f} \cdot \boldsymbol{n} = \frac{Bo_E}{8\pi} \left(\frac{\partial \Phi}{\partial n} \right)^2 . \tag{31}$$

Then from the dimensionless form of the boundary integral equation (20) one can

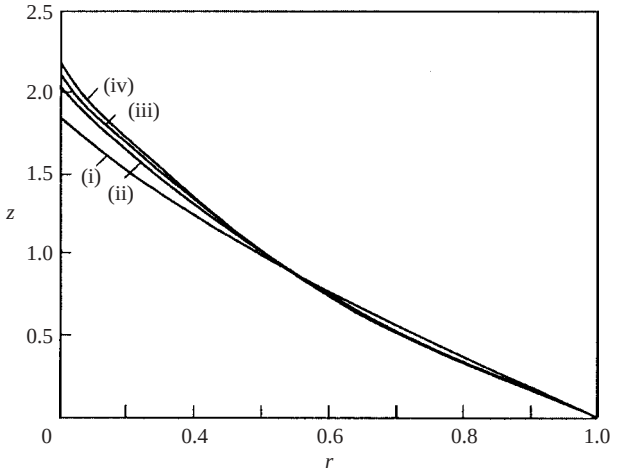

FIGURE 12. The droplet shape at the moment of jet emergence in the case $\alpha_s = \pi/3$. Curve (i) corresponds to $Bo_E = 5.29$, (ii) $Bo_E = 9$, (iii) $Bo_E = 16$, (iv) $Bo_E = 25$.

find the surface velocity to be

$$\boldsymbol{u}(\boldsymbol{x}) = Bo_E \widetilde{\boldsymbol{u}}(\boldsymbol{x}), \tag{32}$$

where the function $\widetilde{\boldsymbol{u}}(\boldsymbol{x})$ does not depend on Bo_E.

Therefore the dimensionless equation of shape evolution becomes

$$\frac{\mathrm{d}\boldsymbol{x}}{\mathrm{d}t} = Bo_E \widetilde{\boldsymbol{u}}(\boldsymbol{x}) \tag{33}$$

(cf. (13)), or

$$\frac{\mathrm{d}\boldsymbol{x}}{\mathrm{d}t_1} = \widetilde{\boldsymbol{u}}(\boldsymbol{x}) \tag{34}$$

with $t_1 = Bo_E t$ (which means that the characteristic time scale is now $\tau_E = \mu/E_\infty^2$ instead of τ_H, as has already been mentioned in § 6 for the case of $Bo_E \gg 1$). Equation (34) does not contain Bo_E. Therefore the droplet shape does not depend on Bo_E when the latter is sufficiently large.

The droplet shapes at the moment of jet emergence can vary widely (see figures 6*b*–9*b*) for the different values of α_s. For $\alpha_s = 0.8\pi$ the shape is vertically elongated and most of the mass accumulates in the leading tip, attached to the plate by a thread (see figure 9*b*). The electric stresses in the tip then far exceed the capillary pressure, but in the thread they are of the same order. Thus the resultant pressure in the thread is much higher than in the tip, which results in strong flow from the thread neck to the tip and the thread is pinched off. Under this scenario a jet is initiated from the moving conical tip later on (cf. figure 9*c*).

For moderate values of α_s when the thread does not form, the absolute value of the velocity decreases very steeply with the distance from the base of the jet. On the characteristic time scale of the jet evolution, the shape of the liquid surface far from the jet remains practically unchanged. The subsequent evolution of the jet cannot be described within the framework of the inertialess approximation because the velocity near the tip becomes too high (cf. § 8).

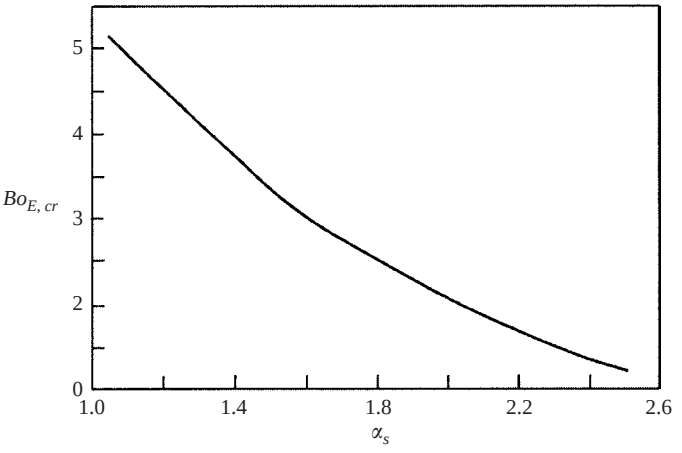

FIGURE 13. Critical electric Bond number versus static contact angle.

It is emphasized that the average semi-angle β of the cone below the jet base in figures 6(*c*)–9(*c*) is approximately 25°–30°. We have not been able to find an approach to the Taylor cone from the subcritical regimes in the present dynamical numerical simulations. The fact that the early supercritical regimes exhibit jets protruding from the cones with $\beta = 25°$–$30°$ favours the assumption that the critical drop configurations (which are very difficult to achieve numerically) are close to those predicted by Yarin *et al.* (2001*b*) with semi-vertical angle of 33.5° than to $\beta_T = 49.3°$. The assumption, however, should be treated with caution, since all the examples in figures 6(*c*)–9(*c*) correspond to slightly supercritical dynamical cases, where semi-angles β can be smaller because of the presence of the protrusion. It should be added that Taylor (1964) and Yarin *et al.* (2001*b*) considered infinite liquid bodies: a cone or a hyperboloid of revolution, respectively. Comparison of these two idealized models with the experimental or less idealized numerical situations, where droplets are finite and attached to a nozzle or a plane wall, should be made with caution. The base parts of the droplets are mechanically affected by the nozzle wall, which restricts the diameter of the droplet (Yarin *et al.* 2001*b*). Such a restriction is, however, much less important for a droplet attached to a plane wall, as in the present case. On the other hand, near the droplet tip any effect of mechanical restrictions and the electric stresses resulting from charge distribution in the areas far from the tip, should be small. That is the reason why both Taylor cones and hyperboloids could be compared with experiments and numerical calculations for finite droplets.

As was mentioned above, the threshold value of the electric Bond number $Bo_{E,cr}$ decreases as the static contact angle α_s increases (figure 13; a similar conclusion could be drawn from figure 31 in Harris & Basaran 1993). This can be explained by the fact that for large contact angles the non-uniformity of the electric field along the surface at $t = 0$ is more significant than in the case of small contact angles, where the droplet is initially rather squat and the electric field is more uniform along the surface. Therefore, in the former case surface pulling by the electric force is relatively stronger and jetting sets in at lower values of Bo_E.

In the case of initial contact angles close to π and sufficiently large values of Bo_E, a third (dripping) scenario of droplet evolution is realized (figure 14). The droplet is slowly stretched in the vertical direction under the action of the electric forces, while most of its mass is concentrated in the leading tip (similarly to the

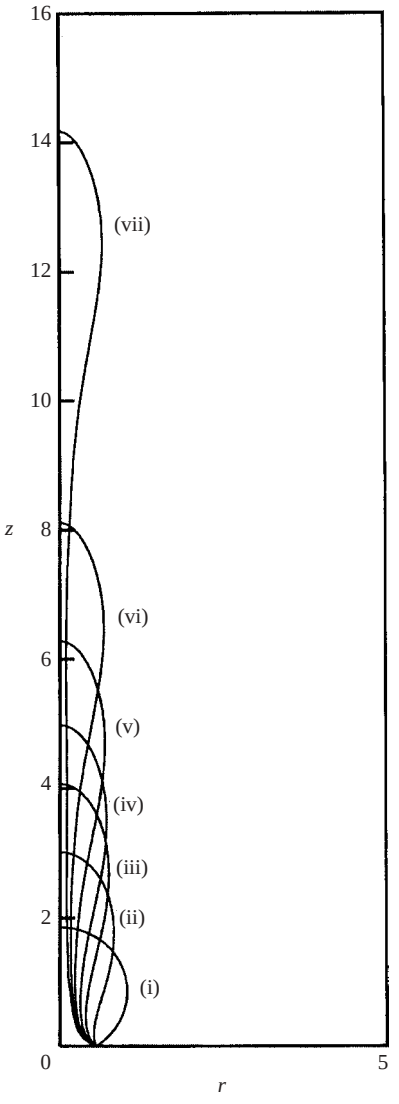

FIGURE 14. Dripping development at the static contact angle $\alpha_s = 0.82\pi$ at $Bo_E = 2.25 > Bo_{E,cr} = 1.13$. (i) $t = 0$, (ii) 1.6, (iii) 2, (iv) 2.1, (v) 2.15, (vi) 2.17, (vii) 2.18.

case shown in figure 9*b*). The tip is attached to the electrode plate underneath by a relatively thin thread. The droplet configurations resemble those associated with gravity-driven dripping (Schulkes 1994) or with drop-on-demand printers (Percin, Lundgren & Khuri-Yakub 1998). Later, the thread is pinched off and the droplet detaches from the electrode, without either a static cone forming or jetting setting in (unlike the case shown in figure 9*b*, *c*).

A critical value of the static contact angle α_{s*} corresponds to the borderline between the second (jetting at $Bo_E > Bo_{E,cr}$) and the third (dripping at $Bo_E > Bo_{E,cr}$) scenarios. The calculations showed that $0.8\pi < \alpha_{s*} < 0.82\pi$. The tip height with supercritical value $\alpha_s \sim 0.82\pi$ is shown in figure 15 versus time for several values of Bo_E. In this case the critical value of the electric Bond number corresponding to the onset of dripping

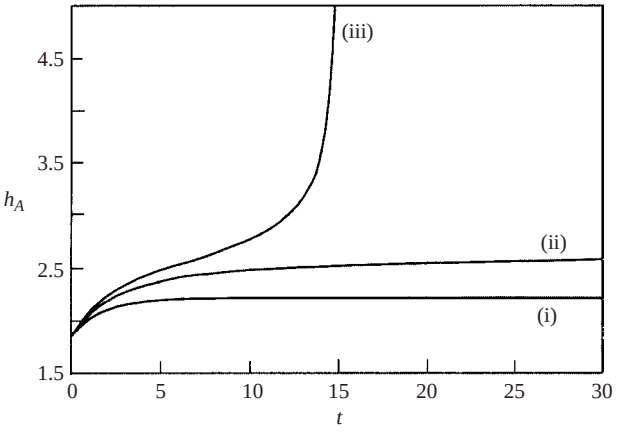

FIGURE 15. The tip height versus time for $\alpha_s = 0.82\pi$. Curve (i) corresponds to $Bo_E = 0.9$, (ii) $Bo_E = 1.12$, (iii) $Bo_E = 1.13$ (cases i and ii subcritical, case iii supercritical dripping).

is $1.12 < Bo_{E,cr} < 1.13$. For $Bo_E \leqslant 1.12$ stable static droplet shapes exist, whereas for $Bo_E > 1.13$ dripping sets in.

8. Straight section of the jet in the supercritical regime

In supercritical regimes electric forces overcome the surface tension, and a static droplet shape cannot be achieved. Then for $\alpha_s < \alpha_{s*}$ jetting originates at the tip. The initial section of the jet (if it is not ruptured due to capillary instability), of the order of several cm, is straight. Further on, when the jet becomes sufficiently thin and its bending stiffness decreases, electrically driven bending instability sets in (Reneker *et al.* 2000). In this section we consider briefly the straight section of the jet.

As mentioned in § 7, the velocity in the jet becomes sufficiently large that the inertialess approximation becomes invalid. Moreover, fast flow reduces significantly the hydrodynamic characteristic time τ_H, which is associated now with the residence time of fluid particles in the jet. The length of the straight part of the jet is of the order of $l \sim 1$ cm and the characteristic velocity there is $V_* = 10^2\,\mathrm{cm\,s^{-1}}$ (Reneker *et al.* 2000). Therefore $\tau_H = l/V_* = 10^{-2}$ s and the ratio $\tau_C/\tau_H = \epsilon V_*/(4\pi\sigma l) = 0.035 \times 10^{-3}$ to 0.035×10^{-2}. The ratio τ_C/τ_H increases even more, since the velocity increases. At high enough values of the ratio τ_C/τ_H the liquid in the jet can no longer be considered as a perfect conductor (as in § 2), but rather as a leaky dielectric (Melcher & Taylor 1969; Saville 1997).

In § 7 it was noted that the cone angle in the transient region, where the viscous inertialess flow transforms into a jet, is $\beta \leqslant 30°$. Then, for a description of the flow in the transient region and the jet it is natural to use the quasi-one-dimensional equations, which has been done in a number of works (Melcher & Warren 1971; Kirichenko *et al.* 1986; Li *et al.* 1994; Ganan-Calvo 1997*a*, *b*, 1999; Cherney 1999*a*, *b*; Stone, Lister & Brenner 1999; Hohman *et al.* 2001*a*; Feng 2002) with different degree of elaboration. The solution of these equations should also be matched to the flow in the drop region. Cherney (1999*a*, *b*) used the method of matched asymptotic expansions to match the jet flow with a conical semi-infinite meniscus. As a basic approximation for the droplet shape the Taylor cone of $\beta_T = 49.3°$ was chosen. This choice seems to be rather questionable in the light of the finding that the Taylor cone represents

a self-similar solution of the Laplace equation to which non-self-similar solutions do not necessarily tend even in the case of a semi-infinite meniscus (Yarin *et al.* 2001*b*). Moreover, even in the situation considered, complete asymptotic matching has never been achieved. Figures 2(*b*), 3 and 4 in Cherney (1999*a*) depict discontinuities in the transition region from the meniscus to the jet. Namely, the solutions for the velocity, the potential and the field strength, and the free-surface configuration are all discontinuous. A similar discontinuity in the distribution of the free-surface charge density is depicted in figure 2 in Cherney (1999*b*). In that work it is mentioned that "rigorous studies of the whole transition region require significant effort and must be a subject of separate work". The rigorous asymptotic matching is not yet available in the literature, to the best of our knowledge. Approximate approaches were tested to tackle the difficulty. In particular, Ganan-Calvo (1997*a*, *b*, 1999), Hohman *et al.* (2001*a*) and Feng (2002) extended the quasi-one-dimensional jet equations through the whole droplet up to its attachment to the nozzle. Such an approach is quite reasonable, but only as a first approximation, since the equations are formally invalid in the droplet region, where the flow is fully two-dimensional. Also, in the electric part of the problem there is a need to take into account the image effects at the solid wall, which is not always done. When done, however (e.g. in Hohman *et al.* 2001*a*), it does not necessarily improve the accuracy of the results. Fortunately, Feng (2002) showed that all the electrical prehistory effects are important only in a very thin boundary layer, adjacent to the cross-section where the initial conditions are imposed (in his case at the nozzle exit). As a result, there is a temptation to apply the quasi-one-dimensional jet equations similar to those of Feng (2002) but moving the jet origin to a cross-section $z_* > 0$ in the droplet (the value of z_* is of the order of the apparent height of the droplet tip).

Our main aim now is matching the flow in the jet region with that in the droplet considered in §§ 2–7. The latter is essentially non-stationary when the jet emerges from the droplet tip, and the acceleration of the particles at the liquid surface increases. This is in response to the action of the increasing-with-curvature normal electric stresses at the droplet surface (note that surface tension essentially does not play any significant role near the droplet tip in this situation). The inertialess theory of § 2, however, overestimates the significance of the fluid acceleration and the transient effects in the region near the droplet tip. It is logical to assume that in the straight section of the jet of the order of several cm (before the bending instability characteristic of electrospinning sets in; Reneker *et al.* 2000) the inertial forces result in a quasi-steady-state flow. On the other hand, the droplet shape close to the jet base continues to be the same as at the moment of jet emergence. The latter assumption is supported by the experimental data (Reneker *et al.* 2000; Yarin *et al.* 2001*b*). The shape of a steady-state jet is determined by the flow rate from the droplet to the jet Q, the applied electric field strength far from the droplet E_∞ (or the corresponding capacitor electric potential difference U), and the liquid properties. Our aim now is to find the quasi-steady-state shape of the jet, as well as its current–voltage characteristic.

At the point where the jet detaches from the droplet z_* the boundary conditions corresponding to matching to the numerically obtained solution found in the droplet were imposed. Namely, the cross-section radius, the slope of the free surface and the surface charge density were matched.

The values of the parameters in the calculations were taken as: $\mu = 200\,\mathrm{P}$, $\gamma \sim 40\,\mathrm{g\,s^{-2}}$, $\rho = 1\,\mathrm{g\,cm^{-3}}$, $\sigma = 9 \times 10^5\,\mathrm{s^{-1}}$ and $\delta = \epsilon/\epsilon_a - 1 = 39$, with ϵ and ϵ_a being the permittivities of the fluid and air, and σ being the fluid conductivity (the leaky dielectric model).

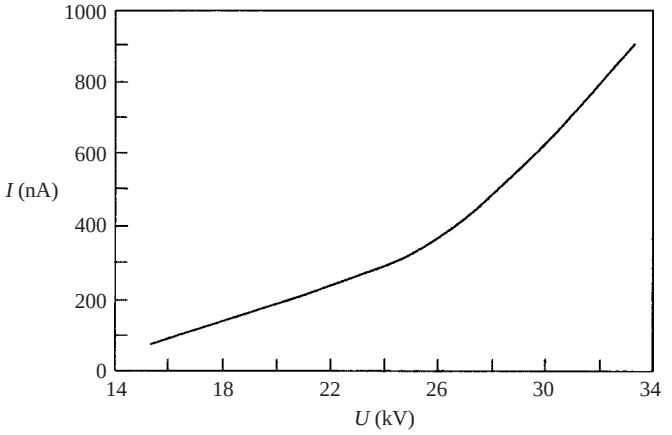

FIGURE 16. The electric current versus the applied voltage for the case $\alpha_s = \pi/3$. The gap between the capacitor plates is taken as 1 cm.

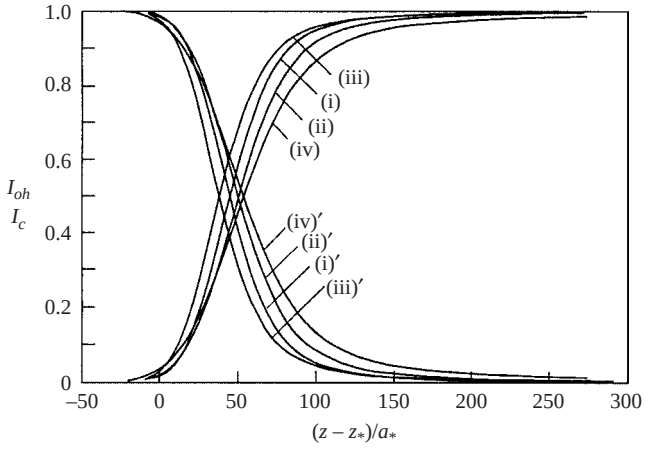

FIGURE 17. The convective and conductive parts of the electric current versus the coordinate z for the case $\alpha_s = \pi/3$. Curves (i) and (i)′ correspond to $Bo_E = 5.29$, (ii) and (ii)′ $Bo_E = 9$, (iii) and (iii)′ $Bo_E = 16$, (iv) and (iv)′ $Bo_E = 25$. Curves without the prime represent the convective part, those with the prime the conductive one.

In the calculations the flow rate from the droplet to the jet Q and the electric current in the jet were found as functions of the applied electric potential difference U. The calculated dependence of the electric current I on the voltage U is shown in figure 16. It is seen that the current increases nonlinearly with the field strength. This results from the fact that over most of the jet length the electric charge is transported convectively and thus differs from the pure ohmic current. The dependence of the dimensionless convective part of the current $I_C = 2qaV/\pi$ and of the conductive ohmic one $I_{Oh} = E_{lz}a^2$ on z is shown in figure 17 for several values of the electric Bond number Bo_E. (The free charge density at the jet surface is denoted by q, the jet cross-section radius by a, the longitudinal velocity by V, and the axial component of the field strength in the liquid by E_{lz}. They are rendered dimensionless by $\epsilon_a E_*/(4\pi)$, a_*, $V_* = Q/\pi a_*^2$ and $E_* = I/(\sigma \pi a_*^2)$, with $a_* = (\epsilon_a Q/4\pi\sigma)^{1/3} \ll a_0$ being the characteristic charge relaxation distance introduced in Fernandez de la Mora & Loscertales (1994).)

It is clearly seen that for all the values of Bo_E the transition from predominantly ohmic to the predominantly convective current takes place at the very beginning of the jet at $0 < (z - z_*)/a_* < 50$, i.e. at the distance of about $50a_*$. This transition from predominantly ohmic current in the droplet region to the convective current in the jet is similar to the findings of Ganan-Calvo (1997*b*) in the context of electrospraying. Note that in the previous models of electrically driven straight jets neither the electric current I nor the volumetric flow rate Q were calculated (Hohman *et al.* 2001*a*; Feng 2002). Instead, these parameters were taken as given which is hard to justify from the physical situation.

It is emphasized that the predicted current–voltage characteristic $I(U, t)$ and the flow rate $Q(U, t)$ are a consequence of the unsteady dynamics of the parent droplet (droplet evolution at the stage when a fully developed jet has been formed is, however, very slow and the time dependence very weak). Thus, both Q and I are the 'dynamic' eigenvalues of the problem for the given initial and boundary conditions, droplet volume and imposed potential difference U. That is the reason why the solution found differs from those published in Ganan-Calvo (1997*b*), where jets issuing from an equilibrium Taylor cone of inviscid fluid were considered in the context of steady-state electrospraying. In that case the issuing flow rate Q compatible with the externally imposed potential U is given and the only eigenvalue is the current I. Ganan-Calvo (1999) showed that I depends on the surface tension γ and the flow rate Q as $I \sim (\sigma Q \gamma)^{1/2}$ and is independent of the applied voltage. Note also that in the present situation, in contrast to electrospraying, the viscous forces are much more important than the surface tension in the region of jet emergence.

9. Summary and conclusions

Three different scenarios of droplet shape evolution in strong electric fields are distinguished, based on the numerical solution of the Stokes equations (by means of the BEM) in perfectly conducting droplets. (i) In sufficiently weak (subcritical) electric fields the droplets are stretched by the electric Maxwell stresses and acquire steady-state shapes where equilibrium is achieved by means of the surface tension. The subcritical range of the electric Bond number given by equation (2) depends on the value of the static contact angle between the droplet and the electrode plate α_s: for $\alpha_s = \pi/3$ we found that $5.14 < Bo_{E,cr} < 5.15$, for $\alpha_s = \pi/2$, $3.03 < Bo_{E,cr} < 3.04$, for $\alpha_s = 2\pi/3$, $1.83 < Bo_{E,cr} < 1.84$, and for $\alpha_s = 0.8\pi$, $1.21 < Bo_{E,cr} < 1.22$. The duration t_E of the evolution to the steady state increases with the electric Bond number Bo_E. For example, for $\alpha_s = 2\pi/3$ we found that $t_E \simeq 8$ for $Bo_E = 1.44$ and $t_E \simeq 20$ for $Bo_E = 1.82$.

(ii) In stronger (supercritical) electric fields with $Bo_E > Bo_{E,cr}$ the Maxwell stresses overcome the surface tension, and jetting sets in from the droplet tip if its static contact angle with the conducting electrode $\alpha_s < 0.8\pi$. In this case the droplet shape (the jet base) acquires a quasi-steady, almost conical shape with the semi-vertical angle $\beta \leqslant 30^\circ$, which is significantly smaller than that of the Taylor cone ($\beta_T = 49.3^\circ$). The droplet shape at the moment of jet emergence is almost independent of the value of Bo_E. The predicted rise of the droplet tip and its overall shape during jetting development agree reasonably with the experimental data of the present work.

The droplet–jet transitional area and the jet region are studied in detail in the framework of the quasi-one-dimensional equations proposed in the literature. In this case the inertial effects and such additional features as the dielectric properties of the liquid (leaky dielectric) are accounted for. The flow in the transitional and

jet regions is matched to that in the droplet. Unlike previous works neither the volumetric flow rate Q nor the electric current in the jet I are assumed. Rather, both Q and I are predicted for a given potential difference U. As a result, the current–voltage characteristic $I = I(U)$ is also predicted. It appears to be nonlinear due to the convective mechanism of charge redistribution superimposed on the conductive, ohmic one. For electric potential differences of the order of 10 kV and fluid conductivity $\sigma = 10^{-4}\,\mathrm{S\,m^{-1}}$, realistic current values of the order of 100 nA were predicted.

(iii) The onset of the third scenario corresponds to the critical value of the static contact angle α_{s*}, found to be close to 0.8π in the supercritical electric fields, namely $0.8\pi < \alpha_{s*} < 0.82\pi$. For $\alpha_s > \alpha_{s*}$ the supercritical electric fields result in detachment of an almost whole droplet similarly to the gravity or drop-on-demand dripping. In particular, for $\alpha_s = 0.82\pi > \alpha_{s*}$, the critical value of the electric Bond number corresponding to the onset of dripping is $1.12 < Bo_{E,cr} < 1.13$. A steady-state shape is reached for $Bo_E < Bo_{E,cr}$, while for $Bo_E > Bo_{E,cr}$ dripping sets in. In this scenario, jetting characteristic of scenario (ii) does not occur.

This research was partially supported by GIF, the German-Israeli Foundation for Scientific Research and Development, Research Grant No I-536-097.14/97, and by the Israel Science Foundation, and the Israel Academy of Sciences, Grant 287/00-1. S. N. R. acknowledges support by the Center for Absorption in Science, Ministry of Immigrant Absorption (State of Israel).

REFERENCES

Bailey, A. G. 1998 *Electrostatic Spraying of Liquid*. Wiley.

Basaran, O. A., Patzek, T. W., Benner, Jr., R. E. & Scriven, L. E. 1995 Nonlinear oscillations and breakup of conducting, inviscid drops in an externally applied electric field. *Indust. Engng Chem. Res.* **34**, 3454.

Becker, A. A. 1992 *The Boundary Element Method in Engineering. A Complete Course*. McGraw-Hill.

Cherney, L. T. 1999*a* Structure of Taylor cone-jets: limit of low flow rates. *J. Fluid Mech.* **378**, 167.

Cherney, L. T. 1999*b* Electrohydrodynamics of electrified liquid menisci and emitted jets. *J. Aerosol Sci.* **30**, 851.

Cloupeau, M. & Prunet-Foch, B. 1989 Electrostatic spraying of liquids in cone-jet mode. *J. Electrostatics* **22**, 135.

Cox, R. G. 1986 The dynamics of the spreading of liquids on a solid surface. Part 1. Viscous flow. *J. Fluid Mech.* **168**, 169.

Driesel, W., Dietzsch, Ch. & Muhle, R. 1996 In situ observation of the tip shape of AuGe liquid alloy ion sources using a high voltage transmission electrone microscope. *J. Vac. Sci. Technol.* B **14**, 3367.

Duft, D., Achtzehn, T., Muller, R., Huber, B. A. & Leisner, T. 2003 Rayleigh jets from levitated microdroplets. *Nature* **421**, 128.

Dussan V., E. B. 1979 On the spreading of liquids on solid surfaces: Static and dynamic contact lines. *Annu. Rev. Fluid Mech.* **11**, 371.

Dzhaugashtin, K. E. & Yarin, A. L. 1977 Numerical simulation of nonself-similar wall jet. *J. Engng Phys.* **32**, 420.

Feng, J. J. 2002 The stretching of an electrified non-Newtonian jet: A model for electrospinning. *Phys. Fluids* **14**, 3912.

Feng, Z. C. & Leal, L. G. 1996 Numerical simulation of the dynamics of an electrostatically levitated drop. *Intl J. Multiphase Flow* **22**, 93.

Fernandez de la Mora, J. 1992 The effect of charge emission from electrified liquid cones. *J. Fluid Mech.* **243**, 561.

Fernandez de la Mora, J. & Loscertales, I. G. 1994 The current emitted by highly conducting Taylor cones. *J. Fluid Mech.* **260**, 155.

Fong, H. & Reneker, D. H. 2000 Electrospinning and formation of nanofibers. In *Structure Formation in Polymer Fibers* (ed. D. R. Salem & M.V. Sussman), vol. 6, pp. 225–246. Hauser, Munich.

Forbes, R. G. & Mair, G. L. R. 1982 Arguments about emitter shape for a liquid-metal field-ion emission source. *J. Phys.* D **15**, L153.

Frenot, A. & Chronakis, I. S. 2003 Polymer nanofibers assembled by electrospinning. *Curr. Opin. Colloid Interface Sci.* **8**, 64.

Ganan-Calvo, A. M. 1997*a* On the theory of electrohydrodynamically driven capillary jets. *J. Fluid Mech.* **335**, 165.

Ganan-Calvo, A. M. 1997*b* Cone-jet analytical extension of Taylor's electrostatic solution and the asymptotic universal scaling laws in electrospraying. *Phys. Rev. Lett.* **79**, 217.

Ganan-Calvo, A. M. 1999 The surface charge in electrospraying: its nature and its universal scaling laws. *J. Aerosol Sci.* **30**, 863.

Harris, M. T. & Basaran, O. A. 1993 Capillary electrohydrostatics of conducting drops hanging from a nozzle in an electric field. *J. Colloid Interface Sci.* **161**, 389.

Haywood, R. J., Renksizbulut, M. & Raithby, G. D. 1991 Transient deformation of freely-suspended liquid droplets in electrostatic fields. *AIChE J.* **37**, 1305.

Hoffman, R. 1975 A study of the advancing interface. I. Interface shape in liquid – gas systems. *J. Colloid Interface Sci.* **50**, 228.

Hohman, M. M., Shin, M., Rutledge, G. & Brenner, M. P. 2001*a* Electrospinning and electrically forced jets: I. Stability theory. *Phys. Fluids* **13**, 2201.

Hohman, M. M., Shin, M., Rutledge, G. & Brenner, M. P. 2001*b* Electrospinning and electrically forced jets: II. Applications. *Phys. Fluids* **13**, 2221.

Huang, Z. M., Zhang, Y. Z., Kotaki, M. & Ramakrishna, S. 2003 A review on polymer nanofibers by electrospinning and their applications in nanocomposites. *Composites Sci. Technol.* **63**, 2223.

Kirichenko, V. N., Petranov-Sokolov, I. V., Suprun, N. N. & Shutov, A. A. 1986 Asymptotic radius of a slightly conducting liquid jet in an electric field. *Sov. Phys. Dokl.* **31**, 611.

Landau, L. D. & Lifshitz, E. M. 1995 *Electrodynamics of Continuous Media.* Pergamon.

Li, H., Halsey, T. C. & Lobkovsky, A. 1994 Singular shape of a fluid drop in an electric or magnetic field. *Europhys. Lett.* **27**, 575.

Melcher, J. R. & Taylor, G. I. 1969 Electrohydrodynamics: a review of the role of interfacial shear stresses. *Annu. Rev. Fluid Mech.* **1**, 111.

Melcher, J. R. & Warren, E. P. 1971 Electrohydrodynamics of a current-carrying semi-insulating jet. *J. Fluid Mech.* **47**, 127.

Mestel, A. J. 1994 The electrohydrodynamic cone-jet at high Reynolds-number. *J. Aerosol Sci.* **25**, 1037.

Mestel, A. J. 2002 Maximal accelerations for charged drops in an electric field. *Phys. Fluids* **14**, 1369.

Michelson, D. 1990 *Electrostatic Atomization.* Hilger.

Notz, P. K. & Basaran, O. A. 1999 Dynamics of drop formation in an electric field. *J. Colloid Interface Sci.* **213**, 218.

Pantano, C., Ganan-Calvo, A. M. & Barrero, A. 1994 Zeroth-order, electrohydrostatic solution for electrospraying in cone-jet mode. *J. Aerosol Sci.* **25**, 1065.

Percin, G., Lundgren, T. S. & Khuri-Yakub, B. T. 1998 Controlled ink-jet printing and deposition of organic polymers and solid particles. *Appl. Phys. Lett.* **73**, 2375.

Pozrikidis, C. 1992 *Boundary Integral and Singularity Methods for Linearized Viscous Flow.* Cambridge University Press.

Prewett, P. D., Mair, G. L. R. & Thompson, S. P. 1982 Some comments on the mechanism of emission from liquid-metal ion sources. *J. Phys.* D **15**, 1339.

Reneker, D. H. & Chun, I. 1996 Nanometer diameter fibers of polymer, produced by electrospinning. *Nanotechnology* **7**, 216.

Reneker, D. H., Yarin, A. L., Fong, H. & Koombhongse, S. 2000 Bending instability of electrically charged liquid jets of polymer solutions in electrospinning. *J. Appl. Phys.* **87**, 4531.

Reznik, S. N. & Yarin, A. L. 2002*a* Spreading of a viscous drop due to gravity and capillarity on a horizontal or an inclined dry wall. *Phys. Fluids* **14**, 118.

Reznik, S. N. & Yarin, A. L. 2002*b* Strong squeezing flow between parallel plates leads to rolling motion at the contact line. *Intl J. Multiphase Flow* **28**, 911.

Reznik, S. N. & Yarin, A. L. 2002*c* Spreading of an axisymmetric viscous drop due to gravity and capillarity on a dry horizontal wall. *Intl J. Multiphase Flow* **28**, 1437.

Reznik, S. N., Zussman, E. & Yarin, A. L. 2002 Motion of an inclined plate supported by a sessile two-dimensional drop. *Phys. Fluids* **14**, 107.

Saville, D. A. 1997 Electrohydrodynamics: The Taylor-Melcher leaky dielectric model. *Annu. Rev. Fluid Mech.* **29**, 27.

Schlichting, H. 1979 *Boundary Layer Theory*, 7th edn. McGraw-Hill.

Schulkes, R. M. S. M. 1994 The evolution and bifurcation of a pendant drop. *J. Fluid Mech.* **278**, 83.

Sherwood, J. D. 1991 The deformation of a fluid drop in an electric field – A slender-body analysis. *J. Phys.* A **24**, 4047.

Shin, Y. M., Hohman, M. M., Brenner, M. P. & Rutlege, G. C. 2001 Electrospinning: A whipping fluid jet generates submicron polymer fibers. *Appl. Phys. Lett.* **78**, 1149.

Sternberg, E. & Koiter, W. T. 1958 The wedge under a concentrated couple: a paradox in the two-dimensional theory of elasticity. *J. Appl. Mech.* **25**, 575.

Stone, H. A., Lister, J. R. & Brenner, M. P. 1999 Drops with conical ends in electric and magnetic fields. *Proc. R. Soc. Lond.* A **455**, 329.

Suvorov, V. G. & Litvinov, E. A. 2000 Dynamic Taylor cone formation on liquid metal surface: numerical modeling. *J. Phys.* D **33**, 1245.

Taylor, G. I. 1964 Disintegration of water drops in an electric field. *Proc. R. Soc. Lond.* A **280**, 383.

Theron, A., Zussman, E. & Yarin, A. L. 2001 Electrospinning field-assisted alignment of electrospun nanofibers. *Nanotechnology* **12**, 384.

van de Vorst, G. A. L. 1994 Modeling and numerical simulation of viscous sintering. PhD Thesis, Eindhoven University of Technology, The Netherlands.

Wohlhuter, F. K. & Basaran, O. A. 1992 Shapes and stability of pendant and sessile dielectric drops in an electric field. *J. Fluid Mech.* **235**, 481.

Yarin, A. L. 2003 *Electrospinning of Nanofibers from Polymer Solutions and Melts*. Lecture Notes No. 5. AMAS Publications, Warsaw.

Yarin, A. L., Koombhongse, S. & Reneker, D. H. 2001*a* Bending instability in electrospinning of nanofibers. *J. Appl. Phys.* **89**, 3018.

Yarin, A. L., Koombhongse, S. & Reneker, D. H. 2001*b* Taylor cone and jetting from liquid droplets in electrospinning of nanofibers. *J. Appl. Phys.* **90**, 4836.

Yarin, A. L. & Weiss, D. A. 1995 Impact of drops on solid surfaces: self-similar capillary waves, and splashing as a new type of kinematic discontinuity. *J. Fluid Mech.* **283**, 141.

Zel'dovich, Ya. B. 1992 *Selected Works of Ya. B. Zel'dovich, Vol. 1, Chemical Physics and Hydrodynamics*. Princeton University Press.

Zeleny, J. 1915 On the conditions of instability of liquid drops, with applications to the electrical discharge from liquid points. *Proc. Camb. Phil. Soc.* **18**, 71.

Zeleny, J. 1917 Instability of electrified liquid surfaces. *Phys. Rev.* **10**, 1.

Zhang, X. & Basaran, O. A. 1996 Dynamics of drop formation from a capillary in the presence of an electric field. *J. Fluid Mech.* **326**, 239.